Verena Reisecker, BSc

Synthesis of NaSICON-type solid electrolytes for Li, Na, K and Ag metal batteries

---

MASTER'S THESIS

to achieve the university degree of
Diplom-Ingenieurin
Master's degree programme:
Technical Chemistry

submitted to
Graz University of Technology

Supervisors:
Univ.-Prof. Dr. Martin Wilkening
Institute for Chemistry and Technology of Materials
Priv.-Doz. Dr. Daniel Rettenwander
Institute for Chemistry and Technology of Materials

Graz, October 2020

AFFIDAVIT

I declare that I have authored this thesis independently, that I have not used other than the declared sources/resources, and that I have explicitly indicated all material which has been quoted either literally or by content from the sources used. The text document uploaded to TUGRAZonline is identical to the present master‘s thesis.

Place, Date

Verena Reisecker

Acknowledgements

At this point I‘d like to thank my supervisors Martin Wilkening and Daniel Rettenwander for giving me the opportunity to be a part of their working group and always providing me with advice and support when needed. In addition I would also like to acknowledge the Austrian Science Fund (FWF, project number P25702) for supporting this thesis financially.

A big thank you also goes out to "Lovely Lukas", who was always lending a helping hand, no matter the number or complexity of problems. I can‘t thank you enough for all the assistance and mental support when syntheses wouldn‘t want to go my way! I´d also like to thank Eveline and Florian for being the best colleagues one could ask for. It sure never got boring in our office! But also to the rest of the working group - thank you for your help and the comfortable working atmosphere.

Additionally, I want to thank my partners in crime Carina, Caroline, Etta and Katharina during this whole journey and for all the precious moments and stories we shared in these past 5 years. I really couldn‘t have done it without you!

Last but not least also a huge thank you to my family, who have always supported me financially as well as mentally during my whole studies.

Abstract

Since their discovery in the 18^{th} century, batteries have come a long way and are now available in various different sizes, shapes and chemistries. They have become an irreplaceable source of electricity in everbody‘s lives, powering small devices like hearing aids and mobile phones, to big-scale appliances like cars and submarines. Due to its numerous benefits compared to other systems, many research teams around the world are focusing on one particular system - the Li-ion battery. However, availability as well as geopolitical concerns about integral components of conventionally available cells demand for alternate possibilities. To pave the way for other battery chemistries, new electrode materials and electrolyte options have to be considered and studied in more detail. One group of solid state electrolytes, that has shown enormously high ionic conductivities as well as outstanding chemical diversity is the group of the Na Super Ionic CONductors (NaSICON), with the general formula of $Na_{1+x}Zr_2Si_xP_{3-x}O_{12}$ (NZSP, 0<x<3).

In particular, the stoichiometry $Na_{3.4}Zr_2Si_{2.4}P_{0.6}O_{12}$ ($Na_{3.4}$ZSP) was shifted into the spotlight after recent investigations have confirmed its high ionic conductivities. Therefore, the focus of this thesis was directed towards the synthesis of the K- and Ag-based analogues *via* solid state route and/or ion exchange, carried out in solution or melt. To allow for analysis of the ion-influence on the crystal structure or dielectric properties of the compound, the Li-based relatives were prepared as well. Several adjustments of the preparation process and the starting mixtures for the K-based materials were carried out, until Powder X-Ray Diffraction (PXRD) and Scanning Electron Microscopy (SEM) measurements could reveal, that the crystal lattice is too tight for the K-ions to fit in. As a consequence, Si was removed from the structure and $KZr_2(PO_4)_3$ (KZP) successfully synthesised *via* solid state route. Afterwards, Electrochemical Impedance Spectroscopy (EIS) measurements of KZP were conducted and the total ionic conductivity (2.04E-10 S/cm) as well as the activation energy (0.83(1) eV) at 230 °C determined. For the Ag-based NaSICON-compound, Simultaneous Thermal Analysis (STA), SEM and EIS measurements could confirm a decomposition of the material in the temperature range of 700 to 800 °C, leading to the segregation of Ag and $ZrSiO_4$ at higher sintering temperatures. In the final ion-exchange experiments, first attempts were made to replace the Na-ions in rhombohedral $Na_{3.4}$ZSP by Ag, K or Li and obtain the respective materials in the same crystal structure. In future investigations, focus needs to be directed towards adapting the crystal lattice to perfectly suit the respective mobile ion and finding an optimum charge carrier concentration.

Kurzfassung

Seit ihrer Entdeckung im 18. Jahrhundert wurden Batterien stetig weiterentwickelt und sind heutzutage in den verschiedensten Größen, Formen und Zusammensetzungen erhältlich. Sie sind ein fester Bestandteil unserer Gesellschaft geworden und speisen sowohl kleine Einheiten wie Hörgeräte und Handys, als auch größere Apparate wie Autos und U-Boote, mit Energie. Aufgrund der vielzähligen Vorteile im Vergleich zu anderen Systemen, fokussieren sich viele Forschungsteams der ganzen Welt auf ein bestimmtes System - die Lithium-Ionen-Batterie. Jedoch verlangen Dendritenwachstum als auch geopolitisch umstrittene Bestandteile der konventionell erhältlichen Akkumulatoren nach alternativen Möglichkeiten. Um den Weg für andere Batteriesysteme zu ebnen, müssen sowohl neue Elektrodenmaterialien als auch Elektrolytoptionen erörtert und analysiert werden. Eine Gruppe an Festkörperelektrolyten, die in der Vergangenheit sowohl vielversprechend hohe ionische Leitfähigkeiten, als auch breite chemische Diversität demonstrieren konnte, ist jene der „Na Super Ionic CONductors" (NaSICON)-basierten Verbindungen, mit der allgemeinen Formel $Na_{1+x}Zr_2Si_xP_{3-x}O_{12}$ (NZSP, 0<x<3).

Speziell die Verbindung $Na_{3.4}Zr_2Si_{2.4}P_{0.6}O_{12}$ ($Na_{3.4}$ZSP) konnte in jüngsten Untersuchungen eine hohe Leitfähigkeit demonstrieren. Daher war der Schwerpunkt dieser Arbeit auf die Synthese der K- und Ag-basierten Vertreter dieser Stöchiometrie mittels Festkörpersynthese und/oder Ionenaustausch in Lösung beziehungsweise Schmelze gerichtet. Um den Einfluss der leitfähigen Ionen auf die Kristallstruktur und die dielektrischen Eigenschaften analysieren zu können, wurden auch die Li-haltigen Verbindungen synthetisiert. Nach mehrfacher Anpassung des Präprationsprozesses und der Startgemische für die Synthese der K-lastigen Verbindungen, konnte schlussendlich anhand von Pulver-Röntgendiffraktometrie-Messungen (PXRD) und Rasterelektronen-Mikroskopie-Aufnahmen (SEM) gezeigt werden, dass das Kristallgitter zu klein ist, um die K-Ionen aufzunehmen. Aufgrund dieser Erkenntnis wurde das Si aus der Stukturformel entfernt und $KZr_2(PO_4)_3$ (KZP) erfolgreich mittels Festkörpersynthese hergestellt. Anschließend wurden mittels Elektrochemischer Impedanzspektroskopie (EIS) die totale ionische Leitfähigkeit (2.04E-10 S/cm) sowie die Aktivierungsenergie (0.83(1) eV) bei 230 °C bestimmt. Die PXRD-, Thermische Analyse- (STA) und SEM-Messungen der Ag-haltigen Verbindung konnten bestätigen, dass eine Zersetzung der Verbindung im Temperaturbereich zwischen 700 und 800 °C stattfindet, wobei sich Ag und $ZrSiO_4$ bei höheren Sintertemperaturen abscheiden. In finalen Ionenaustauschexperimenten wurden erste Versuche unternommen, das Na-Ion in rhomboedrischem $Na_{3.4}$ZSP durch Ag, K oder Li zu ersetzen, mit dem Ziel die jeweiligen Materialien in der selben Kristallstruktur zu erhalten. Bei zukünftigen Untersuchungen muss der Schwerpunkt darauf gelegt werden, das Kristallgitter perfekt an das jeweilige mobile Ion anzupassen und eine optimale Ladungsträgerkonzentration zu finden.

Contents

1 Introduction

1.1 Significance of batteries in society & need for improvement

In the past decades, increased efforts have been paid to the research and development of electrochemical storage systems.[1,2,3,4,5] The most promising representatives of this genre are rechargeable batteries, which can provide clean, affordable and reliable energy output.[1,6] However, the system to provide all of these properties at once, has yet to be found. Their broad area of application ranges from the implementation in stationary electrochemical storage installations to the use in portable electronic devices, like mobile phones or laptops.[1]

Batteries show a high degree of chemical and architectural diversity, with one of the most important and extensively studied one being the Li ion battery.[1,2,3] Li metal exhibits numerous benefits compared to other anode materials, like low-weight, a high specific capacity being 3862 mAh/g, as well as the most negative electrode potential of -3.05 vs. SHE, leading to superior specific energies in the range of 600 Wh/kg. Unfortunately, the implementation of pure Li metal poses the risk of a thermal runaway as a result of dendrite-formation. This is why so-called Li-intercalation materials are applied in current conventional Li-ion batteries.[1] However, Li as well as other metals like Co, which are key components in these cells, are already a subject of geopolitical concerns.[7]
But not only the choice of electrode material influences the performance of a battery. The electrolyte between the two electrodes, which takes care of the ion exchange during charging/discharging, is a substantial component of these devices and has a significant impact on their efficiency and power outcome. Due to the reactive nature of Li-containing substances, aprotic liquid electrolytes have to be applied in current Li-ion cells, which are typically composed of a solvent, conductive salt and additives.[1] The main drawback of organic electrolytes is their characteristically high volatility and flammability. To eliminate this potential source of danger and improve the reliability of batteries, inorganic solid state electrolytes can be used.[8,9,10,11]

Therefore, besides improving the already mature Li-technology, another path of research is directed towards so-called post Li-ion batteries, which concentrate on different mobile cations (e.g. Na^+, K^+, Mg^{2+}, Ca^{+2}) and make use of a metal anode, a high-voltage cathode and a solid electrolyte.[8,12,13]

1.2 Benefits & challenges of all solid state batteries

The setup of solid state batteries is rather simple, as depicted in the following scheme 1.1. It consists of two solid electrodes, the anode (=negative electrode) and the cathode (=positive electrode), which are spatially separated by a solid electrolyte, typically made of a polymeric or ceramic material.[11,14,15] During discharging, ions are extracted from the positive electrode and move through the electrolyte to the negative electrode. Simultaneously, the corresponding

amount of electrons is exchanged via an external circuit in the same direction. During charging, this process is reversed.[11]

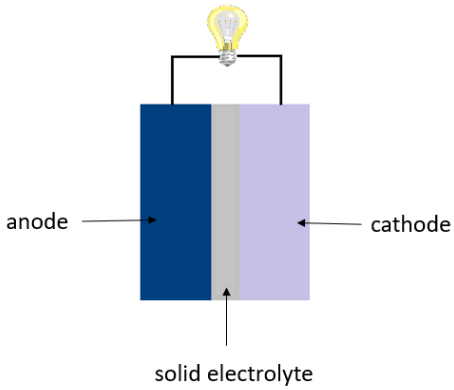

Figure 1.1: Schematic setup of a solid state battery

Inorganic solid electrolytes show a variety of advantages, which could lead to an eventual replacement of organic electrolytes in conventional batteries. The most important ones are:[8,16]

+ **safety**: preliminary results of thermal and mechanical investigations look very promising, electrolytes are inflammable and non-volatile, possible damages of the battery case do not result in leakage of the electrolyte
+ **lifetime**: due to slower reactivity of solid compounds, superior cycling performance could be observed, a variety of ageing effects is directly connected to liquid electrolytes
+ **operation regime**: solid state electrolytes allow for an extensive temperature window, where liquid electrolytes would freeze, boil or even decompose
+ **energy density**: higher densities of solids allow for greater energy densities of solid state batteries
+ **new materials**: metal anodes like Li, Na or Mg are applicable, in combination with high voltage cathodes, higher capacities should be accessible

But also the application of solid state electrolytes does not solve all existing problems of current wet cells. Recent investigations show, that dendrite growth is not only exclusive to liquid electrolytes, but can also happen in solid ones.[17,8] Another challenge is the stabilisation of the interface between electrolyte and electrode. These peripheral zones often exhibit different structural and compositional properties compared to the bulk materials and interfere with ionic conduction or may even promote electronic conductivity.[8] Although the architecture and volume of solid state batteries can be adapted and tailored more easily compared to liquid cells, the loss of physical contact at the interface represents a problem. This effect is induced by the volume changes during cycling and can lead to the formation and propagation of microcracks or also a delamination of the interface.[8,15]

In order to meet the rising world energy demand and provide superior specific capacity, as well as higher energy density and safety, further scientific studies in the field of solid state electrolytes have to be carried out.[8,9,15]

1.3 NaSICON-type solid electrolytes

1.3.1 Definition & chemical diversity

One of the most important and highly investigated candidates for future solid state electrolytes are the so-called NaSICON materials.[4,18,19] This term generally stands for **Na S**uper **I**onic **CON**ductors and corresponds to a family of materials that exhibit the following chemical formula:[4]

$$Na_{1+x}Zr_2Si_xP_{3-x}O_{12} \ ; \ 0<x<3$$

This system, short-termed NZSP, was first discovered by Hong and Goodenough, who published their work on the synthesis and consequent analysis of these compounds in 1976.[20,21] Their reports additionally showed, that the Na-ions are reversibly exchangeable with other cations (e.g. Ag^+, K^+, Li^+), which has led to numerous following studies with all kinds of different substitutions. Today, the term NaSICON is used to describe all phosphates with the generic formula AMP_3O_{12}.[4,22] The following Table 1.1 gives an overview about already reported, possible substitutions of the sites A and M.

Table 1.1: Possible, reported occupations of sites A and M in AMP_3O_{12}[4,22]

cations	**A**	**M**
monovalent	Li^+, Na^+, K^+, Rb^+, Cs^+, Ag^+, H^+, H_3O^+, $NH_4{}^+$	-
divalent	Mg^{2+}, Ca^{2+}, Sr^{2+}, Ba^{2+}, Cu^{2+}, Pb^{2+}, Cd^{2+}, Mn^{2+}, Co^{2+}, Ni^{2+}, Zr^{2+}	Cd^{2+}, Mn^{2+}, Co^{2+}, Ni^{2+}, Zr^{2+}
trivalent	Al^{3+}, Y^{3+}, La^{3+}, Lu^{3+}	Al^{3+}, Ga^{3+}, In^{3+}, Sc^{3+}, Ti^{3+} V^{3+}, Cr^{3+}, Fe^{3+}, Y^{3+}, La^{3+} Lu^{3+}
tetravalent	Ge^{4+}, Zr^{4+}, Hf^{4+}	Si^{4+}, Ge^{4+}, Sn^{4+}, Ti^{4+}, Zr^{4+} Hf^{4+}, V^{4+}, Nb^{4+}, Mo^{4+}
pentavalent	-	V^{5+}, Nb^{5+}, Ta^{5+}, Sb^{5+}, As^{5+}

In addition to the A- and M-site, also the P-atom can be partially exchanged for elements like Si, Ge or As. As one can see, the combination of these various elements offers an incomparable degree of chemical diversity.[4] The initial system $Na_3Zr_2Si_2PO_{12}$ (in the following referred to as Na_3ZSP) already showed promising ionic conductivities, being $6.70 \cdot 10^{-4}$ S/cm at 25 °C.[21] Since then, various adjustments concerning the stoichiometric composition and microstructure have been made to increase this value.[4,18,22,23] For the composition $Na_{3.4}Zr_2Si_{2.4}P_{0.6}O_{12}$ ($Na_{3.4}ZSP$), a bulk conductivity of $1.5 \cdot 10^{-2}$ S/cm at 25 °C has been reported.[18]

1.3.2 Structure & conduction pathway

The high ionic conductivity of these materials results from their three-dimensional framework, constructed of corner-sharing PO_4-tetrahedra and MO_6-octahedra,[4] as depicted in the following Figure 1.2 for NZSP on the left-hand side (A).[24] Depending on the stoichiometry, the cations can then fill the formed octahedral cavities to a certain extent.[25] In general, NaSICON materials can adapt rhombohedral, monoclinic or also triclinic (only few examples - therefore excluded in further introduction) phases.[4]

The highest ionic conductivities have been reported for the rhombohedral phase $R\text{-}3c$,[20,26] where the Na-ions can occupy two different interstitial sites (only for $x > 0$). At the first site (1), the Na-ion is connected to O-ions of three tetrahedra below and above, whereas the one placed at the second site (2) is six-fold connected to O-ions of coplanar tetrahedra. NZSP exhibits this phase, except for the compositional range of $1.8 \leq x \leq 2.2$, where the structure is distorted to form a monoclinic phase of lower symmetry. Here, an additional third site (3) is introduced, where the Na-ion is three-fold connected to the O-ions of three ZrO_6-octahedra.[4] Figure 1.2 gives an overview of such a Na-ion network in a rhombohedral (pink) and monoclinic (blue) phase in the middle section (B).[24]

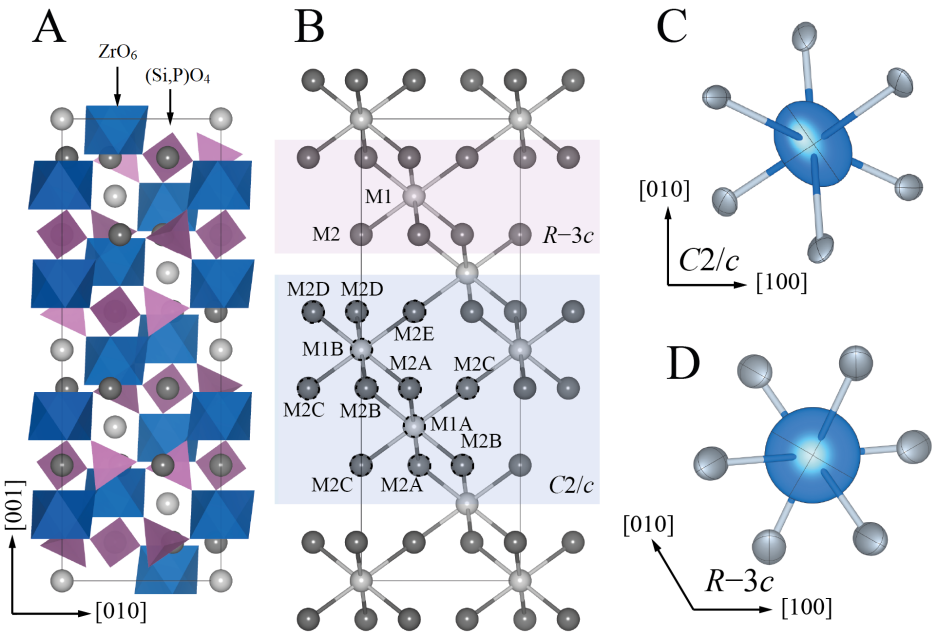

Figure 1.2: (A) 3D framework of $Na_3Sc_2(PO_4)_3$ and $Ag_3Sc_2(PO_4)_3$ (SG = $R\text{-}3c$); (B): interconnection of atoms (modified graph) (C,D) equivalent displacement parameters for the Na-ions in the monoclinic and rhombohedral phase[24]

The additional graphics C and D visualise the corresponding equivalent displacement parameters for $C2/c$ and $R\text{-}3c$, respectively. Conductivity is induced by the Na-ions jumping from one interstitial site to another.[4] The geometrical shape of this parameter gives information about where the Na-ions are most likely to be found and therefore a possible preferential conduction pathway can be determined. As one can see, the monoclinic phase exhibits an ellipsoidal shape, whereas the rhombohedral one is spherically formed, meaning, that the $C2/c$ structure shows a favoured diffusion direction, whereas the $R\text{-}3c$ does not.[24]

Figure 1.3 visualises how conduction takes place in the rhombohedral (a) and the monoclinic (b) phase of NaSICON-type materials through the oxygen triangles T1 (red) and T2 (black).[27] The jumping distance between the interstitial sites is around 3 Å and depends on the chemical and stoichiometric composition.[4] For the bigger triangle T2, the Na-movement through the skeleton structure is more facilitated, whereas for the smaller triangle T1, it is slowed down. This trend can be derived from the activation energies for the corresponding processes and tells us, that the size of this formed bottleneck has a crucial impact on the ionic conductivity in NaSICON materials.[28]

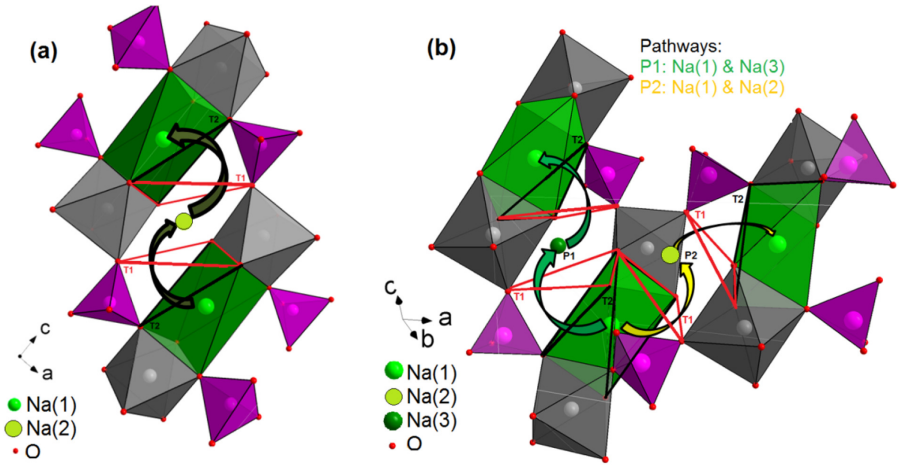

Figure 1.3: Schematic representations of the triangles T1 (red) and T2 (black) where Na-conduction takes place in (a) rhombohedral $NaZr_2(PO_4)_3$ and (b) monoclinic Na_3ZSP; pink tetrahedra = PO_4, green octahedra = NaO_6, grey octahedra = ZrO_6[27]

1.3.3 Dependency of ionic conduction

Ionic conductivity in NaSICON-type materials is influenced by various different parameters, which will be elucidated and discussed in more detail in the following paragraphs.

Composition

The survey of the transport properties of sodium conductor-type materials from Tietz *et al.*[4] gives an overview about numerous Na-containing NaSICON compounds and their corresponding conductivities at room temperature (RT) as well as at 300 °C. It shows, that the choice of cations at the A- and M-sites, as well as the stoichiometry, influence the ionic diffusion enormously. The dependency of the effective mean ionic radius was analysed and could be determined to have an optimum at around 0.72 ± 0.1 Å. Figures far from this value have shown an exponential decrease in ionic conductivity. But not only the elemental composition is of relevance, as also for different stoichiometries a change in conduction can be observed. Generally, it can be stated, that an increase in the charge carrier concentration also leads to an increase in conductivity. In reality however, at some point a maximum concentration is reached, resulting from phase changes or also from a half-filled occupancy of the charge carrier sites.[4] Graph 1.4 shown below once more visualises the explained trends.

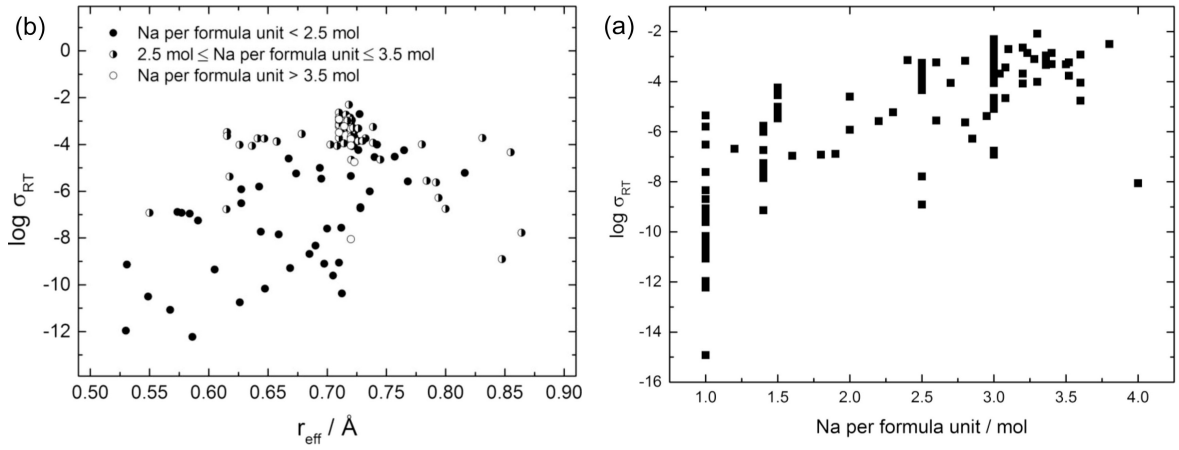

Figure 1.4: Correlation of effective mean ionic radius (a) and stoichiometric composition of Na-containing NaSICONs (b) with ionic conductivity[4]

Phase changes

Depending on the stoichiometric composition and the temperature, NaSICON-type materials can exhibit different structures, with the most prominent one being the rhombohedral and monoclinic space groups, as already mentioned in subsection 1.3.2. Typical phase transition temperatures for Na-based compounds lie in the range of 400 ± 200 °C. In earlier days, studies concentrated on high temperature solid state batteries and therefore a lot of information is only available at 200 to 300 °C.[4] Due to the different activation energies of the space groups, an extrapolation of the conductivity to room temperature is sometimes not possible and leads to falsified data.[4,18]

Another issue in earlier days was the separation of bulk and grain boundary conductivity. Therefore, the conductivities discussed in these reports also include contributions from grain boundaries and side phases. But even today, the determination of the high frequency response sometimes poses challenges and can only be observed with highly advanced technology at very low temperatures.[18]

Microstructure and porosity

Another two important aspects, that most of the times are missing in earlier papers, are the microstructure and porosity of prepared and measured pellets.[4] This information is especially crucial for further application of these materials in solid state batteries, where high density, sufficient mechanical strength as well as good interfacial contact are of utmost importance to ensure high power output and cycling stability.[8,15] Important aspects concerning the fabrication of these solid electrolytes are the mechanical mixing processes as well as the temperature programmes applied. Additionally, the presence of side phases in the samples can lead to an increase in the resistivity and therefore reduce the conductivity.[29]

1.4 Motivation

NaSICON materials could be a key element in revolutionising future energy storage systems.[4,18,10] The combination of their potential for high ionic conductivities with their structural flexibility, seems to make this class of materials one of the top-suitable candidates for the application in beyond Li-ion batteries.[18] Their performance can be improved by optimising the composition, phase and microstructure.[4] However, in published literature, lots of information is missing on high-frequency processes and microstructural aspects, like the porosity of prepared pellets. In addition, at the time special focus was paid to compositions ranging from $2.8 \leq x \leq 3.2$, as it was believed that these would show the highest conductivities. Due to all these reasons, further synthesis and more detailed characterisation of NaSICON materials have to be carried out to enable their application in future solid state batteries.[18]

The goal of this master's thesis was the substitution/replacement of Na in NZSP by K, Li, and Ag, to potentially find further attractive solid state electrolytes and also to analyse how the ion conductive phase behaviour changes with the mobile ion involved. The greatest effort was paid to the development of the K-containing NaSICON compounds, as K could be an underrated element for future solid state batteries. Hong and Goodenough were the first ones to give insight into the crystal structure of K-substituted materials like $K_3Zr_2Si_2PO_{12}$.[21] Interestingly since then, only few reports have dealt with this group of compounds. At the moment, Na-batteries are a hot topic, as Na is cheap, abundant and geopolitically not questionable.[3] But also K shows such favourable properties.[30] Additionally, it exhibits an even more negative electrochemical potential being -2.93 V vs SHE., which is closer to Li (-3.05 V vs. SHE) compared to Na (-2.71 V vs. SHE).[1,31] In the past years, significant progress was made in this category of batteries concerning electrode materials as well as organic electrolytes.[30,32,33,34]

Another mobile ion that could be interesting for the realisation of future solid state batteries is Ag. Over the past decades, different types of Ag-based fast ion conducting compounds have been reported, ranging from crystalline ionic conductors like AgI, to doped polymers and amorphous glass ionic conductors.[35,36,37,38] Besides their high stability as well as conductivities at even ambient temperatures, they also exhibit outstanding storage abilities. Until now, the application of Ag-based ionic conductors is however limited to primary batteries.[37,39]

Despite some of their drawbacks as explained in section 1.1, Li-based batteries will remain one of the most relevant energy storage systems, especially in the portable electronics section. Compounds of type $LiM_2(PO_4)_3$ (M= Hf, Zr, Ge, Ti, Sn) have already proven an extensive electrochemical stability window as well as sufficient chemical stability at ambient conditions.[40,41] One of the highest-conducting representatives of this class is $LiTi_2(PO_4)_3$ as well as its Al-doped derivative $Li_{1-x}Al_xTi_{2-x}(PO_4)_3$. However, upon contact with the Li anode, the material easily degrades and Ti(IV) is reduced to Ti(III). Zr-containing analogues on the other hand, demonstrated much higher stabilities against metallic Li, and its decomposition products additionally show ionic conductivity.[42,43,44]

2 General Aspects

The following sections will give a short insight into solid state chemistry concerning the classification and packing of crystals, presence of defects and explain how diffusion generally takes place in solid materials. Additionally, the most extensively used analysis methods concerning the characterisation of the samples will be discussed in more detail.

2.1 Crystal structures & packing of solids

Solid state chemistry in general deals with the synthesis, analysis and application of inorganic, crystalline materials. Crystal chemistry not only comprises all information of the unit cell (dimensions and positions of atoms) but also integrates data of the elements like their oxidation states, ionic radii, coordination requirements as well as preferences concerning their bonding situation.[45]

The crystal lattice can be described as a regular arrangement of atoms in three dimensions, whose smallest repetition is known as the so-called "unit cell". This cell exhibits the full symmetry of the crystal structure, and can be categorised according to its axial lengths and angles into **seven crystal systems**, which are visually represented in Figure 2.1 below.[45]

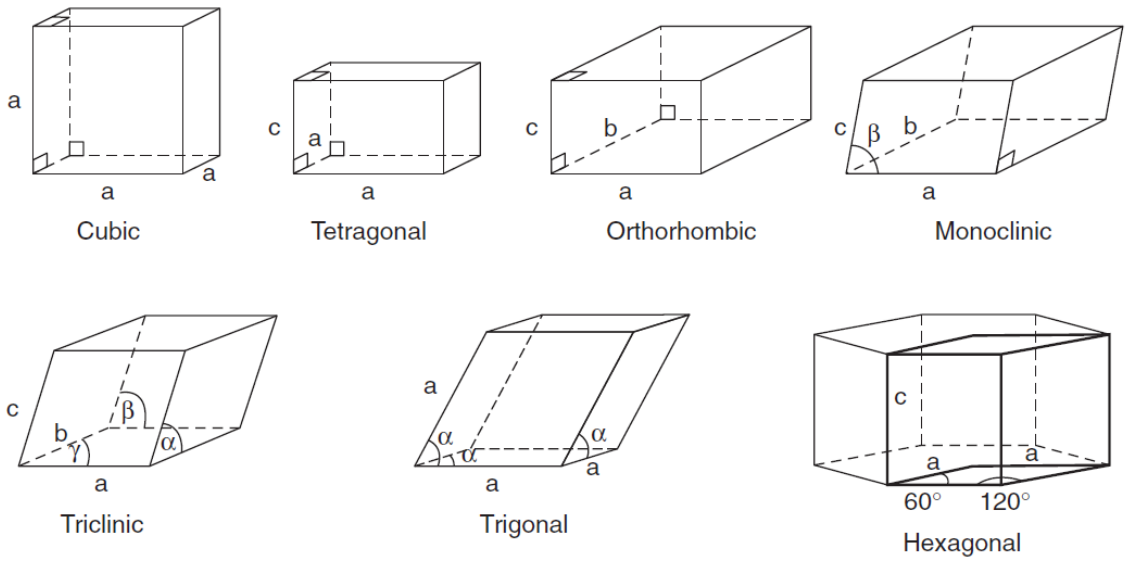

Figure 2.1: The seven crystal systems[45]

All crystallographic shapes, can be sorted into one of these seven crystal systems. It is important to point out, that they do not define the crystal structure.[45] They are just imaginary building blocks that help us to simplify the aggregation of molecules/ions in the solid material.[46]

A more correct way to characterise crystal systems, is by the presence or absence of symmetry elements.[45,47] The following Table 2.1 once more summarises the relationships between the corresponding parameters and additionally gives an overview of the symmetry elements observed in each system.

Table 2.1: Geometrical data & symmetry elements found in the corresponding system, *also termed rhombohedral[45]

system	geometries	symmetry description
cubic	$a = b = c$; $\alpha = \beta = \gamma = 90\,^\circ$	four threefold axes
tetragonal	$a = b \neg c$; $\alpha = \beta = \gamma = 90\,^\circ$	one fourfold axis
orthorhombic	$a \neq b \neq c$; $\alpha = \beta = \gamma = 90\,^\circ$	three twofold axes / mirror planes
monoclinic	$a \neq b \neq c$; $\alpha = \gamma = 90\,^\circ$	one twofold axis / mirror plane
triclinic	$a \neq b \neq c$; $\alpha \neq \beta \neq \gamma \neq 90\,^\circ$	none
trigonal*	$a = b = c$; $\alpha = \beta = \gamma \neq 90\,^\circ$	one threefold axis
hexagonal	$a = b \neq c$; $\alpha = \beta = 90\,^\circ$, $\gamma = 120\,^\circ$	one sixfold axis

The reason why symmetry elements are more reliable, when characterising a certain crystal structure, is, that some crystals can possess pseudo-symmetry. This means, that its unit cell may exhibit the right geometries for a certain system, but not the corresponding essential symmetry elements. The unequal-sign in the geometrical description section of Table 2.1, therefore has to be seen as a "must not", rather than a "can not".[45]

The symmetry elements used to describe crystal structures can be grouped into point and space symmetry as shown in Table 2.2.

Table 2.2: Symmetry elements used to describe the unit cell[45]

Point symmetry	Space symmetry
mirror plane	glide plane
rotation axis	screw axis
inversion axis	
alternation axis	
centre of symmetry	

Elements of point symmetry like mirror planes, rotation and inversions axes, always leave one point unchanged during the symmetry operation (e.g. atom located at the centre of symmetry).[45] Finite-sized molecules only exhibit this type of symmetry elements and their combination gives rise to 32 point/crystal groups. Crystals can also exhibit an additional set of symmetry operations, formed by the combination of translation and simultaneously one of the point elements to form glide and screw planes. In total, this leads to 230 space groups, needed to describe the full internal periodicity of the lattice.[45,47,48]

In certain cases, the primitive unit cell is not suitable to display the full symmetry of the crystal structure. However, since it is still easier to work with unit cells, centring was included, which gives rise to a total of 14 Bravais lattices. By face-, body- or base-centring, additional lattice points are included in the way the name indicates.[45]

Sometimes, information on just the unit cell itself may still not be enough to get a full insight into the 3D structure of a compound. One common way of visualising and describing such structures is based on **close-packing**. This kind of visualisation technique cannot be applied to all, but a lot of solid materials and is based on the principle of highest density. In general, there are two main ways of close-packing: cubic and hexagonal.[45]

If we consider an atom to look like a perfectly-shaped sphere, the densest 2D sheet of these spheres is achieved by leaving as less empty space between them as possible. Figure 2.2 shows, how the atoms can be most closely packed in 2D (a) and additionally gives an example of a non cp-arrangement (b). The second layer is now added such, that the spheres take up as much of the hollow space induced by the first layer as possible (picture c or d).[45]

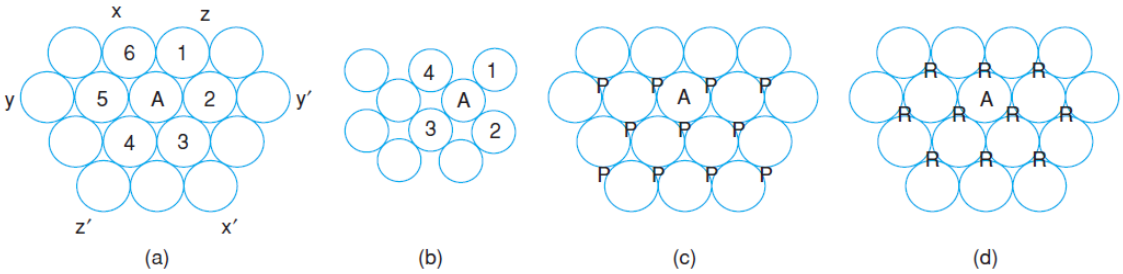

Figure 2.2: (a) Densest possible arrangement of equally sized atoms in 2D; (b) non-cp layer (c,d) examples of stacking the second layer in a dense way[45]

Up to this point, both of the two structures look identical. The way the third layer is now added on top of this stack makes the essential difference. For the hexagonal close-packing, the next layer is added at the identical x/y-positions of the A-sheet, to form an ABABAB sequence. If the atoms of the third layer are placed at a new position C to form an ABCABCABC sequence, cubic close-packing is obtained as illustrated in Figure 2.3.[45,49]

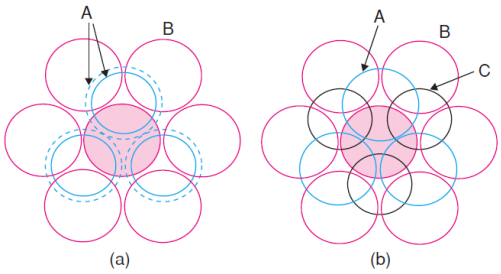

Figure 2.3: Coordination number of 12 in the (a) hexagonal ABAB-stacking and (b) cubic ABCABC-stacking[45]

The arrangement of these spheres gives rise to tetrahedral and octahedral voids between adjacent layers, which could fit spheres of sizes 0.225r and 0.414r, respectively (with r being the radius of the bigger close-packed spheres). Besides the closely-packed structures, there are also less densely-packed ones, like the body-centred or simple cubic structure.[49]

2.2 Defects

Although it is practical to look at all solids as perfect crystal systems, such ideal configurations do not exist at accessible temperatures ($T \neq 0$ K). Every solid material shows mistakes or deviations concerning the periodicity of the lattice, which is overall described as a defect. The source of such defects can be numerous, as atoms vibrate at temperatures unequal to 0 K. Some may be displaced, further impurity atoms may be included in the system or also stacking faults can disturb the ordered arrangement. The introduction of such errors requires a certain amount of energy, which is called the enthalpy (or more precisely here change in enthalpy) ΔH, but also increases the entropy ΔS, since e.g. a misplaced atom can occupy a variety of different sites. The dependency of this occupation probability W on the entropy is explained by the Boltzmann equation 2.1 (with k_B being the Boltzmann constant):[45]

$$S = k_B \cdot lnW \tag{2.1}$$

With the introduction of defects, the term $T\Delta S$ will exceed ΔH and therefore the overall free energy ΔG of the system decreases, as one can deduce from the following equation 2.2.

$$\Delta G = \Delta H - T\Delta S \tag{2.2}$$

At a certain concentration of defects, the total energy will increase again, since the lattice is already quite disordered and ΔH exceeds the value of $T\Delta S$. Figure 2.4 shows how the corresponding contributions change in energy as a result of the rising number of defects and increasing temperature.[45]

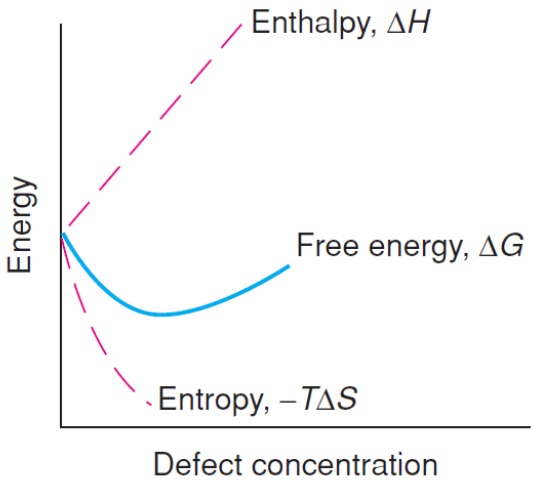

Figure 2.4: Simplified graphical representation of the relationship between entropy, energy and defect concentration[45]

Defects can generally be grouped according to their stoichiometry or geometry. In the first case, one can distinguish between stoichiometric/intrinsic defects, where the crystal chemistry remains unchanged, and non-stoichiometric/extrinsic defects, which result from chemical alterations. In

the second case, the dimensionality of the defect is used for classification, such that all of them can be assigned either to point, line or plane defects.[45] Although all of these defects occur in solid materials, the following text will only concern **point defects**, since these are of prime importance for the understanding of later considerations in this thesis.

It was around the 1930s, when scientists like Schottky, Wagner and Frenkel investigated these so-called "classical defects" and their origins in more detail.[45] Figure 2.5 shows, how the corresponding errors affect the periodicity of the crystal structure. A Schottky defect describes the absence of cations and anions in a perfect crystal system by the "introduction" of vacancies (left-hand side), whereas Frenkel defects concern the displacement of certain atoms, which then occupy an interstitial site in the crystal lattice (right-hand side).[45,50]

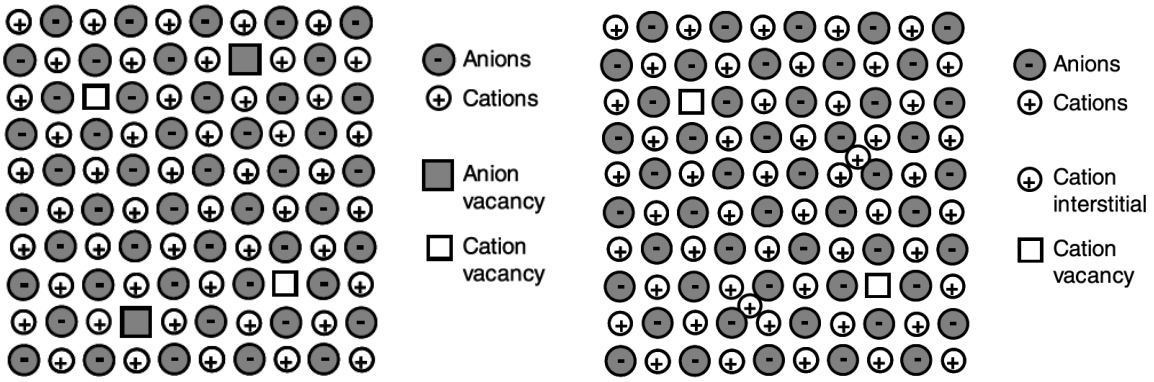

Figure 2.5: Introduction of Schottky (left) and Frenkel (right) defects in a crystal lattice[50]

In both cases, the electroneutrality of the system is preserved.[45,50] Often, such solid materials are doped with foreign atoms that differ in valency, to alter the conductivity of the material. Accordingly, the concentration of defects has to be increased to maintain an overall charge of zero.[50] If the concerned ions are of equal size, Schottky defects will dominate, whereas if they show an adequate difference in diameter, Frenkel defects will be predominantly found.[49]

However, one has to distinguish between classical ionic compounds and fast ion conductors (solid electrolytes), where an open structure allows for the transport of small ions.[50] Corresponding considerations will be discussed in the following section 2.3.

2.3 Diffusion in solids

2.3.1 Fick's laws

Some of the most pioneering work concerning the diffusion of solids was done by Alfred Fick. First records date back to 1855, where he could find a relation between the flux of certain particles (molecules, atoms or ions) J and their concentration c. Putting them into a mathematical context, allows for the determination of the proportionality constant, the so-called diffusion coefficient D:

$$J_x = -D \cdot \left[\frac{\partial c}{\partial x}\right] \tag{2.3}$$

The negative sign is introduced to take the opposite directions of D and J into account. The diffusion coefficient is usually given in length squared per time [m^2/s] and contains information about the process of concentration equalisation in a given system. The relationship displayed in equation 2.3 can also be applied to a three dimensional system by introducing the Nabla operator ∇:

$$J = -D\nabla c \tag{2.4}$$

If a system is influenced by additional processes/factors like chemical reactions, external fields or high-diffusivity paths leading to anisotropy, the corresponding relationships shown above get more complicated. When combining the law above with the equation of connectivity, the diffusion can be described as a function of time according to Fick's second law:[50]

$$\frac{\delta c}{\delta t} = \nabla \cdot (D\nabla c) \tag{2.5}$$

2.3.2 Random walk & atomic jump processes

By additionally taking the physical quantities of the diffusing particles into account, Albert Einstein and Marian Smoluchowsky were able to connect the diffusion coefficient with the mean square displacement of the corresponding particles. In general, the diffusion of particles in a certain solid material can be imagined as a so-to-say random walk, where e.g. ions hop from one position in the lattice to another. By introducing defects in the crystal system, diffusion can be enhanced or induced. Additional factors influencing independent jumps of particles are the hopping distance as well as the jump rates. This dependency is mathematically explained by the Einstein-Smoluchowsky equation:[50]

$$D = \frac{\langle R^2_{x,y,z} \rangle}{6\tau} \tag{2.6}$$

where $R_{x,y,z}$ indicates the total displacement (in x, y and z direction) and τ the time needed for the jump. The jump distance d usually exhibits values in the order of the next neighbour distance a, which is in turn dependent on the crystal system present. Therefore, the mean

residence time $\bar{\tau}$ of an atom at a certain lattice position can then be described as a function of the atomic coordination number Z and the jumping rate Γ according to 2.7:

$$\bar{\tau} = \frac{1}{Z\Gamma} \tag{2.7}$$

A certain diffusional pathway may be favoured over others, when "diffusion vehicles", like vacancies, are present in the system. In this case, an additional parameter, the correlation factor *f*, has to be introduced, that accounts for such dependent diffusive motions.

If we go back to equation 2.7, one can see that for certain crystal systems, diffusive motion is more facilitated compared to others. However, diffusion can still be enhanced for a given crystallographic arrangement, if the jumping rate is increased. When looking at a simple atomic jump process as illustrated in Figure 2.6, it can be seen that the particle has to move through the small channel between two neighbouring lattice points, to get from one interstitial site (A) to another (B). This diffusional motion thereby follows an Arrhenius-type of behaviour. At low temperatures, the particle vibration is barely enough to overcome the energy barrier G^M (Gibb's free energy of migration M, see equation 2.2), whereas at elevated temperatures, the additional amount of thermal energy promotes the jump.

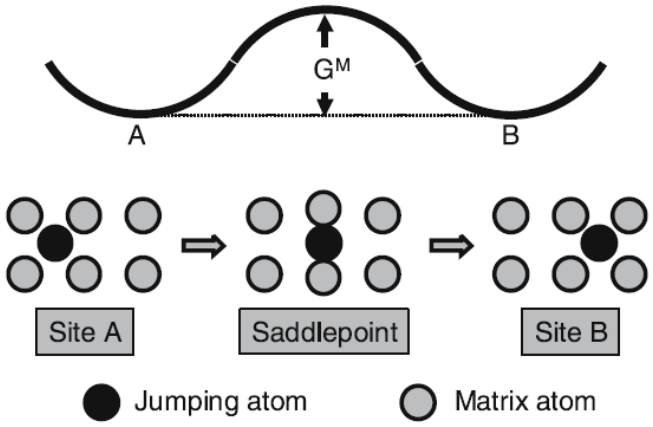

Figure 2.6: Jumping process depicted in an energy landscape[50]

The relationship between the jump rate ω and the attempt frequency ν_a, can be described as follows:

$$\omega = \nu_a^0 exp\left(-\frac{G^M}{k_B T}\right) = \left(-\frac{H^M}{k_B T}\right) = \left(-\frac{S^M}{k_B T}\right) \tag{2.8}$$

The value of ν^0 is in the order of the Debye frequency (typically lies between 10^{12} and 10^{13} s^{-1}) and describes the vibration frequency at the equilibrium site.[50]

2.3.3 Diffusion mechanisms

In general, there are several ways how diffusion can take place in solid materials. In the following text however, only the three selected mechanisms will be discussed shortly.

In the **interstitial mechanism**, a solute of smaller particle size compared to the solvent atom occupies interstitial sites and can move through the lattice by atomic hopping, as already explained in subsection 2.3.2. A sequence of such atomic jumps can be seen in Figure 2.7 on the left-hand side. The highest strain is induced at the saddle point, however, the diffusing particles are normally so small that they can easily jump from one site to another, without greatly distorting the lattice. Also, defects are no necessary prerequisite for the interstitial atoms to migrate through the system, and therefore such particles usually show rather high diffusion coefficients.

For the **vacancy mechanism**, defects have to be present in the corresponding solid, such that particles can migrate through the crystal by filling a neighbouring vacancy. This effect is graphically depicted in Figure 2.7 on the right-hand side. Especially in close-packed structures, this motion is more favoured than e.g. direct exchanges.[50]

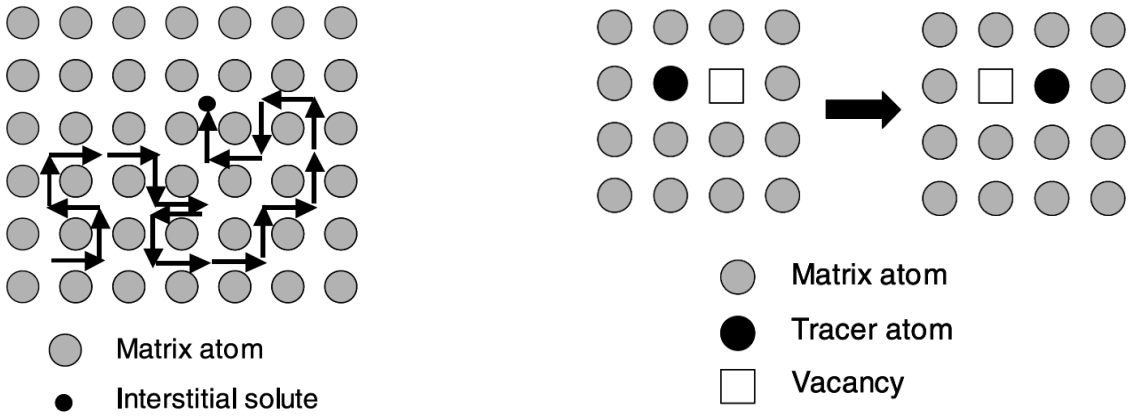

Figure 2.7: Interstitial (left) and vacancy (right) mechanism in a solid[50]

These classical diffusion models are however unfit to explain the ion transport characteristics of super-ionic conductors like the NaSICON-type materials. By using *initio modelling*, He *et al.*[51] were able to conclude, that diffusion does not take place by isolated ion hopping events like it does in many other solids, but can be explained in form of a low-barrier-**concerted mechanism**. This can be traced back to the strong interactions and unique configurations of the mobile ions. The high number of mobile ions exceeds the amount of low energy sites, such that some have to occupy sites of higher energy. The latter ones are however stabilised by Coulomb interactions from the neighbouring mobile ions, thereby lowering the migration barrier. This eventually allows multiple ions to hop simultaneously to a neighbouring site and is the source for the high ionic conductivities in this class of materials.

2.4 X-Ray Diffraction

2.4.1 Miller indices and lattice planes

Any simple crystallographic structure can be visually divided into a set of atom planes. These in turn are often related to the unit cell of the solid, such that it e.g. overlaps with any of the faces, or (which is more likely) coincides with it. By introducing such sheets, it becomes more easy to refer specific atoms in the structure to a reference grid. A certain arrangement of atoms can be divided into planes of different orientation, which also has an influence on the inter-spatial distance d, as shown in Figure 2.8 on the left-hand side.

In order to describe the spatial arrangement between these planes and the unit cell, the Miller indices hkl were introduced. To assign a certain plane, a number of steps have to be carried out:

- step 1: choose one atom as the corner of the unit cell and set it to 0, this is now the origin of the Cartesian coordinate system, with the directions being (hkl), which is identical to (xyz)
- step 2: take the intersections of the adjacent plane with the axes h, k and l; the maximum distance between two atoms is 1, if the plane intersects one face at half height it is therefore labelled as 1/2
- step 3: clear the fractions to obtain integers and write them as (hkl)

The determination of the Miller indices is exemplified in Figure 2.8 on the right-hand side.

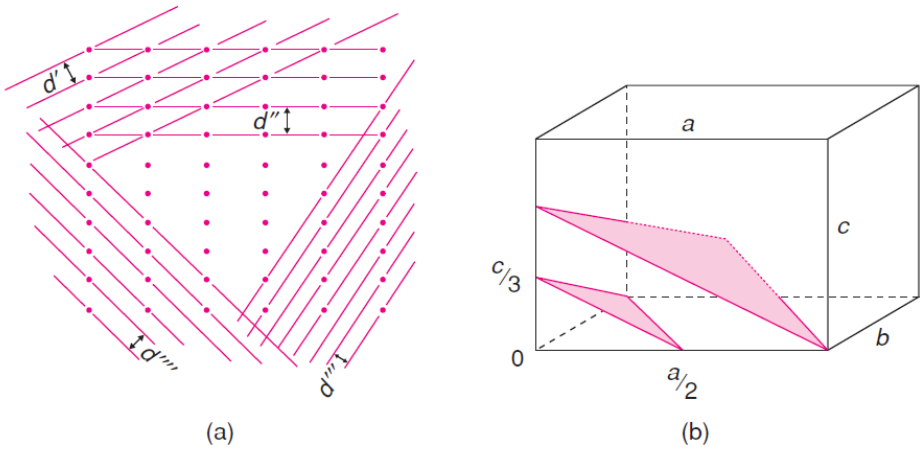

Figure 2.8: (a) d-Spacings between rows of different planes; (b) determination of Miller indices[45]

If the three coordinates are placed in {}-brackets, they stand for a set of equal planes like for example (100), (010) or (001) in the cubic crystal system. In addition, they can also be used to specify a certain direction, in this case they are shown in []-brackets. In some cases, it can also be useful to consider negative directions. Therefore, an additional bar is placed above the corresponding index.[45] The special attraction of this coordinative system is its ability to simplify certain crystal calculations,[47] as well as its possible application to all crystal systems, except for the hexagonal one, where an additional 4th index is needed.[45]

As already mentioned before, the d-spacing is the shortest distance between two adjacent parallel planes. With the coordinative system (hkl) being introduced, it is now possible to calculate this value for a given crystal system like for the orthogonal cell shown in equation 2.9:

$$\frac{1}{d_{hkl}^2} = \frac{h^2}{a^2} + \frac{k^2}{b^2} + \frac{l^2}{c^2} \tag{2.9}$$

The lower the symmetry of the crystal system, the more complicated this equation gets, as each angle unequal to 90 ° introduces an additional variable.[45]

Another important aspect is the density of the unit cell, which becomes accessible by determination of the volume V and the number of formula units Z in the cell. When additionally considering the formula weight FW and the Avogadro constant N, the density can be calculated according to equation 2.10:

$$\rho = \frac{FW \cdot Z}{V \cdot N} = \frac{FW \cdot Z \cdot 1.66}{V} \tag{2.10}$$

This value can be of high interest in solid state synthesis, as it allows for a verification of the crystal data as well as a determination of one of the other three parameters. Also, it can give information on the microstructure, concerning its porosity and defect origin or concentration, by comparison of the calculated value D_{calc} with the empirically determined one D_{obs}.[45]

2.4.2 Diffraction at crystals

Diffraction at crystals can be explained analogously to diffraction of light at an optical grating. Therefore, radiation in the size of the d-spacing between the planes, which usually adapts values ranging from 2-3 Å, is needed to irradiate the crystals. Although electrons or neutrons could be used for this matter, the typically chosen source of radiation are X-rays emitted from Cu (λ = 1.5418 Å). When the rays hit the atoms or ions of the crystal, the radiation gets diffracted in a specific way. This phenomenon was first described by Laue and Bragg.

Laue was capable of relating the diffraction at crystals to the diffraction of light and therefore was able to derive a relation between the separation a, the wavelength of the radiation λ and the diffraction angle θ. For a 3D arrangement of atoms this yields:[45]

$$\begin{aligned} a_1 \cdot sin(\theta_1) &= n \cdot \lambda \\ a_2 \cdot sin(\theta_2) &= n \cdot \lambda \\ a_3 \cdot sin(\theta_3) &= n \cdot \lambda \end{aligned} \tag{2.11}$$

In order for diffraction to occur at a certain atom/ion, all of these equations must be fulfilled. Although, these are mathematically correct and can be applied to analyse diffraction processes, it is much easier to work in reciprocal space with Miller indices, like explained by **Bragg**. Here, diffraction takes place at a lattice point as pictured in Figure 2.9.

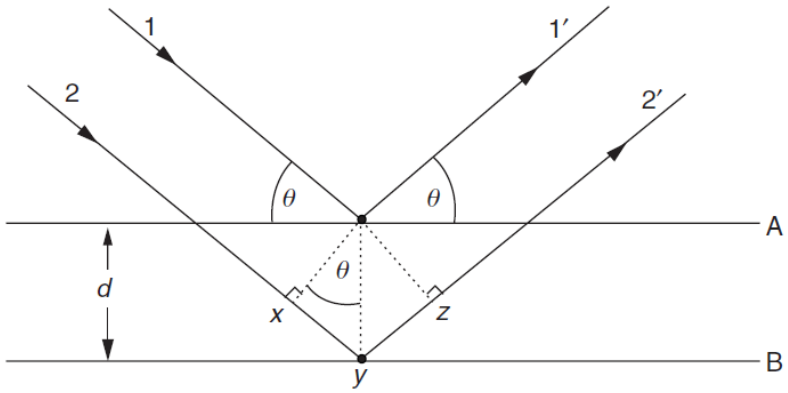

Figure 2.9: Reflection of X-rays at an optical grating[45]

When X-rays hit a certain plane (A) at the right angle and position, they get reflected with the angle of the incident wavelength. The ones that pass through the first layer, can then be reflected by the layer underneath (B) and so forth. All the reflected waves exiting the sample, show the same reflecting angle and are therefore parallel. By taking the extra path into account, that the second wave has to travel in contrast to the first one (xy + yz), the following relations can be set up (identical to Laue):[45]

$$\begin{aligned} xy = yz &= d \cdot sin(\theta) \\ xyz &= 2d \cdot sin(\theta) \end{aligned} \tag{2.12}$$

$$2d \cdot sin(\theta) = n \cdot \lambda \tag{2.13}$$

Equation 2.13 gives the final Bragg relation, where d stands for the smallest distance between the two planes, θ for the angle of reflection (= Bragg angle), λ for the wavelength of the radiation and n for the order of reflection, an integer number.[45,52] A Bragg-reflected beam is only observed, when the reflected beams are in phase such that constructive interference can occur. At all other angles, the waves are out of phase and destructive interference/cancellation occurs.[45]

2.4.3 Analysis of crystal structures *via* PXRD

Powder X-Ray Diffraction (PXRD) is one of the most common techniques to quantitatively analyse the crystal structure of solid materials and phases. X-rays are created by thermal emission from a metal (e.g. Cu), filtered and directed at a finely pulverised powder, where crystals are ideally randomly distributed. At least some of those crystals have to be aligned at the right angle such, that diffraction can occur. The positions and intensities of these reflections are then measured *via* a strip of photographic film or movable detector as shown in the simplified scheme below.[45]

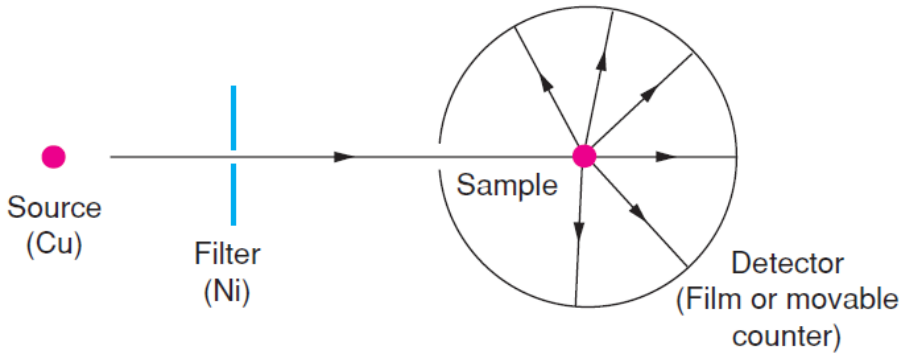

Figure 2.10: Simplified set-up of a PXRD device[45]

The outcome of these measurements is displayed by plotting the normalised intensity signal against the position in terms of 2 θ. This way, a unique pattern of reflexes is obtained for each phase or crystal structure, that acts like a fingerprint. However, when carrying out measurements, a few limitations of this technique have to be noted:[45]

- if the material in question is not entirely phase-pure, it exhibits additional signals from these impurities/side phases that can complicate or even prohibit a correct assignment of the reflexes
- if the structure analysed, is closely related to another set of almost identical patterns, identification of the right phase can get very difficult
- no differentiation can be made between materials of variable stoichiometric composition or solid solutions from a single pattern

The higher the symmetry of a certain crystal structure, the lower the amount of reflexes observed in the XRD pattern. This effect is based on the principle of multiplicity. In the cubic crystal for example, the line h00 exhibits a multiplicity of six (h00, h00, 0k0, 0k0, 00l, 00l), whereas in less symmetric structures like the tetragonal or orthogonal one, it is four and two, respectively. As a result, the number of peaks increases, whereas the intensity of the signals decreases.[45] Lots of materials, like the NaSICON family, show phase changes at higher temperatures.[4] These order-disorder phenomena most of the times lead to different intrinsic properties of the samples and to correlate these features to the structural framework of the material is of essential interest in solid state chemistry.[45]

2.5 Impedance

Electrochemical Impedance Spectroscopy (=EIS) has become one of the most important characterisation methods in the field of wet and solid state electrochemistry, as it is an indestructible in-situ method that gives insight into frequency-dependent processes.[53,54,55,56,57,58] It can be used to study all kinds of solid state compounds, ranging from superionic conductors to electrical insulators.[54] Since in this master's thesis, the application of this method is restricted to NaSICON ceramics, the following explanations will mainly concentrate on the field of single-ion-conducting solid state materials.

2.5.1 Principle of AC Impedance Spectroscopy

The simplest way of measuring the AC response of a system, is to directly apply an excitation signal to the cell and measure the resulting system response in a certain frequency range. The Impedance Z in general is dependent on the voltage U and the current I at a certain time t according to equation 2.14:[54]

$$Z = \frac{U_t}{I_t} \tag{2.14}$$

The obtained value Z usually comprises data of resitive (R) as well as reactive (inductance L/ capacitance C) components. By defining the voltage as a sinusoidal signal, where ω stands for the angular frequency:

$$U = U_0 \cdot sin(\omega t) \tag{2.15}$$

a non-linear system response is measured:

$$I = I_0 \cdot sin(\omega t \cdot \Phi) \tag{2.16}$$

The impedance is reflected by the amplitude amplification and the phase shift Φ, which is $\neq 0$ in case the system does not behave like an ideal resistor.[54] Thus, it is dependent on the frequency, and therefore able to reveal underlying chemical processes. By defining the phase shift as an angle, Z can be written as a complex number according to equation 2.17:[54,59,55]

$$Z = Z' + j \cdot Z'' \tag{2.17}$$

where Z' stands for the real part, Z" for the imaginary part (and j for the imaginary unit $\sqrt[2]{-1}$), which contain information on the magnitude and direction of the signal. From this information-rich signal, lots of other complex parameters can be extracted like the admittance, electric modulus or also the permittivity.

The different regions in the analysed systems are usually characterised by parallel connection of the resistance R and capacitance C. The product of such a RC-circuit element yields the

characteristic time of the respective process and since these processes are separable the frequency at maximum loss ω_{max} can be calculated according to the following relationship:[54,59]

$$\omega_{max} \cdot RC = 1 \tag{2.18}$$

For homogeneous systems only one RC-circuit is needed to describe the underlying processes. However, not all compounds can be described by a single RC-element. Polycrystalline materials like ceramics for example, are represented by a serial connection of RC-elements, like in a two-phase system, as shown in graph 2.11. For some materials, the ideal resistive and capacitive elements have to be "mixed" in order to describe the measured AC response properly. Therefore, a number of distributed impedance elements like for example the constant phase element (CPE) have been introduced.[54]

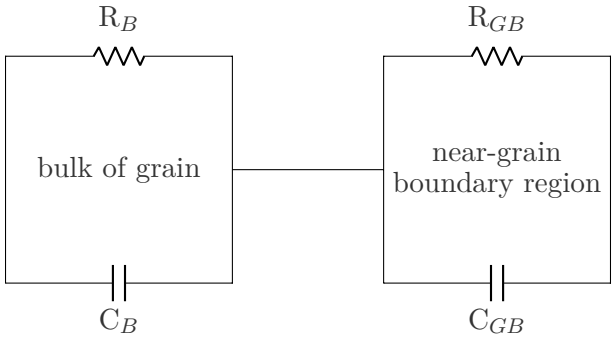

Figure 2.11: Schematic representation of an equivalent circuit used to describe polycrystalline materials, adapted from reference[60]

Determination of the respective capacitance values most of the times allows for the separation of different physical processes in the material investigated. The following Table 2.3 gives an overview of commonly observed phenomenons and their capacitance ranges. A trend that is clearly observable in this listing is, that the smaller the values (e.g. 10^{-12} for bulk), the higher the volume fraction. This correlation helps to simplify later assignments of the contributions.[54]

Table 2.3: Possible interpretations of capacitance values[54]

Capacitance [F/cm]	**Possible Phenomenon**
10^{-4}	electrochemical reactions
10^{-5} - 10^{-7}	sample-electrode interface
10^{-7} - 10^{-9}	surface layer
10^{-9} - 10^{-10}	bulk ferroelectric near Curie-T
10^{-8} - 10^{-11}	grain boundary
10^{-11}	minor, second phase
10^{-12}	bulk

By rephrasing equation 2.17 shown before to equation 2.19:

$$Z = (1/R_1 + j\omega C_1)^{-1} + (1/R_2 + j\omega C_2)^{-1} \tag{2.19}$$

the separation of the individual RC elements can be mathematically carried out according to equations 2.20 and 2.21:[54]

$$Z' = R_1/\{1 + (\omega R_1 C_1)^2\} + R_2/\{1 + (\omega R_2 C_2)^2\} \tag{2.20}$$

$$Z'' = R_1[\omega R_1 C_1/\{1 + (\omega R_1 C_1)^2\}] + R_2[\omega R_2 C_2/\{1 + (\omega R_2 C_2)^2\}] \tag{2.21}$$

2.5.2 Graphical representation of data

The output of impedance measurements can be plotted in various different ways.[55] Most of the times, the obtained data is visualised in form of a complex plane, where the imaginary part *Z"* is plotted against the real part *Z'*. For simplification and aesthetic reasons, the sign of the imaginary part is reversed to obtain all capacitive data in the first quadrant of the coordinative system.[58] The magnitude of frequency decreases from left to right and each point obtained, contains information of the impedance at a certain frequency.[56] This kind of graphical representation is called a **Nyquist plot**.[58] An illustration of such graphs can be found in the following Figure 2.12.

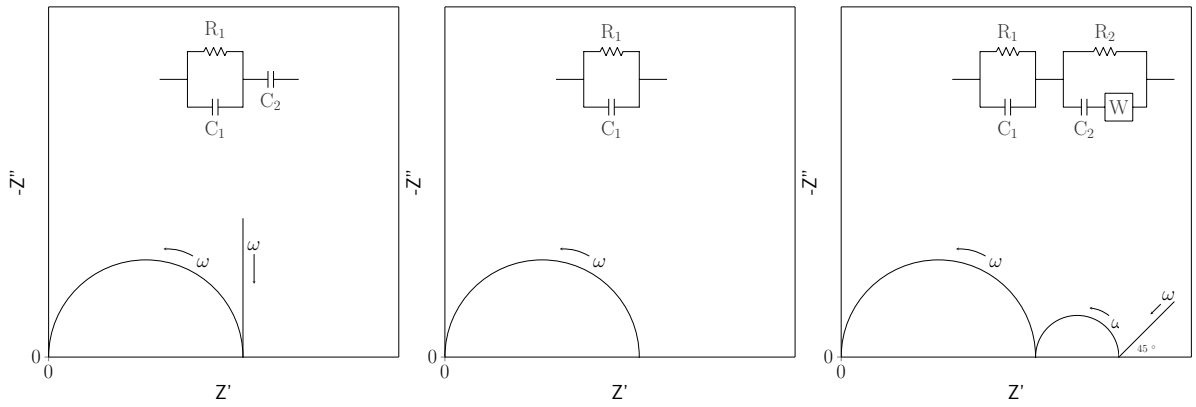

Figure 2.12: Visualisation of complex impedance and related equivalent circuits for a) single crystal ionic conductor with blocking electrodes, b) non-blocking/reversible electrodes which show electronic conduction, c) infinite, Warburg-type ionic diffusion; adapted from reference[54]

The frequency at the maximum of this half-circle, which can be used to determine C_0, can be described by the following relation:[55]

$$f_{Z''max} = \frac{1}{2\pi R C_0} \tag{2.22}$$

The total resistance R_T of the system is given by the intersection of the half-circle with the x-axis at lower frequencies. Depending on how many processes are taking place in a certain system, several semi-circles may be obtained, where one can follow the other or also overlap. In both cases, the respective component values are accessible. For the first one, determination is facilitated as each time constant and therefore semicircle can be treated separately. In the

second case, graphs can get quite complicated and evaluation of the corresponding contributions is only possible by e.g. iterative curve fitting or deconvolution.[55]

Another way to differentiate between bulk and grain boundary contributions of the total conductivity is to plot the real part of the conductivity σ' against the frequency ν in a double-logarithmic way to give a **conductivity isotherm** as shown in Figure 2.13.[61] This kind of representation is especially useful to analyse the dependency of the conductivity on the temperature.[62]

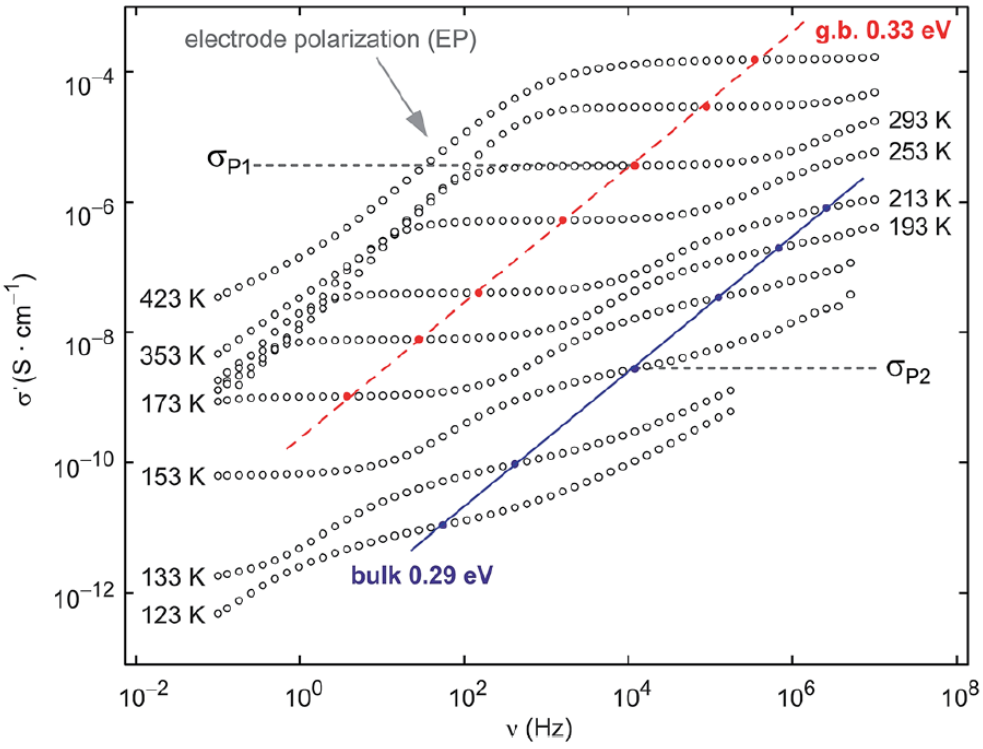

Figure 2.13: Conductivity isotherm of a sintered LATP pellet[62]

At very high frequencies, the curve represents a dispersive conductivity due to the back-and forth-motion of atoms at short time scales ($\hat{=}$ higher frequencies).[63,64] At larger time scales ($\hat{=}$ lower frequencies), a DC conductivity plateau can be observed that corresponds to long-range ion transport. At even lower frequencies, the electrode polarisation is detectable. The spectrum also points out, that not all contributions are necessarily detectable at each temperature. Here, the bulk contribution is only visible at very low temperatures, whereas at the higher temperatures only the grain boundary share is observable.[62]

Since the observed phenomena follow an Arrhenius-type law,[64] the following relationship can be deduced:

$$\sigma_{DC} = \frac{\sigma_0}{T} exp\left(\frac{-E_a}{k_B T}\right) \tag{2.23}$$

where σ_0 stands for the infinite temperature limit of the DC conductivity, T for the temperature

and E_a for the activation energy of the diffusion process.[65] As one can derive from this equation, the DC conductivity increases with increasing temperature, which can also be empirically observed in Figure 2.13.[63] Additionally, this relationship allows for the determination of the activation energy of the corresponding processes.[62]

2.5.3 Problems associated with this technique

Many people encounter difficulties during the evaluation of impedance spectra, as they show information-rich, complex curves. A certain basic knowledge of mathematics like Laplace, Fourier transforms and complex numbers is necessary to understand the influences of the corresponding parameters on the shape of the Impedance curve.[53] Even for separated contributions, errors in calculations can occur that lead to falsified data.[55] Besides, measurements of low frequency processes are time-consuming and even with state-of-the-art instruments, low frequency processes may not be demonstrable.[57]

3 Experimental Section

3.1 Equipment & Chemicals used

The following lists contain all devices and chemicals that were used for the preparation and characterisation of the synthesised substances.

3.1.1 Equipment

- Ball mill, FRITSCH Pulverisette 7
- Megafuge 1.0, Heraeus
- MSK-110 Hydraulic Press, MTI Corporation
- Oven, Nabertherm
- High vacuum sputter coater, Leica EM QSG100
- Ultra Plus Field – Emission Scanning Electron Microscope, Zeiss
- X-ray diffractometer, Rigaku MiniFlex
- X-ray diffractometer, Bruker D8 Advance
- Simultaneous Thermal Analyser, Netzsch 449 F1 + Quadrupole Mass Spectrometer, Netzsch 403 C
- Broadband dielectric analyser, Novocontrol Concept 80
- Grinding and polishing machine, Struers

3.1.2 Chemicals

- Sodium carbonate (99.9 %), Sigma-Aldrich
- Potassium carbonate, Sigma-Aldrich
- Lithium carbonate ($\geq$ 99 %), Sigma-Aldrich
- Ammonium dihydrogen phosphate, Merck
- Silicon dioxide, Sigma-Aldrich
- Zirconium(IV)oxide (99 %), Sigma-Aldrich
- Niobium(V)oxide, Merck
- Silver nitrate (99+ %), Merck
- Silver nitrate solution 1M, Merck
- Potassium nitrate (99 %), Merck
- Lithium nitrate (> 98 %), Merck

3.2 Preparation of Ag-, K-, Li & Na-containing NaSICON ceramics

3.2.1 Solid state synthesis of K-based NaSICONs

Throughout this thesis, several different adjustments were made concerning the solid state synthesis route of the K-containing NaSICON-type materials. Therefore, the following Subsubsection 3.2.1 will give a detailed description of the initial, major route, while Subsubsection 3.2.1 will describe the different alterations made afterwards.

Major route

Step 1 - Homogenisation

For the preparation of the NaSICON ceramics $K_3Zr_2Si_2PO_{12}$ (K_3ZSP), $K_{3.4}Zr_2Si_{2.4}P_{0.6}O_{12}$ ($K_{3.4}$ZSP) and $K_{3.36}Zr_{1.96}Nb_{0.04}Si_{2.4}P_{0.6}O_{12}$ ($K_{3.4}$ZSP (2%Nb)) *via* solid state synthesis, stoichiometric amounts of K_2CO_3, ZrO_2, SiO_2, $NH_4H_2PO_4$ and Nb_2O_5 were weighed in for a total batching size of around 5 g. The respective powder was then transferred to a ZrO_2-grinding jar (45 mL), equipped with 10 mL ethanol as well as 180 ZrO_2-balls (⌀ 5 mm), and milled in a high energy planetary ball mill from Fritsch. The applied programme is displayed in Table 3.1.

Table 3.1: Settings for ball milling of the K-containing materials *before* the calcination process

parameter	description
speed [rpm]	500
time [min]	10
pause [min]	10
cycles [#]	72
revers	off

Step 2 - Calcination

Afterwards, the powder was dried, transferred to an alumina crucible and subjected to the following temperature programme shown in Figure 3.1. The first annealing step was introduced to allow for decomposition of $NH_4H_2PO_4$ and consequent evaporation of NH_3.

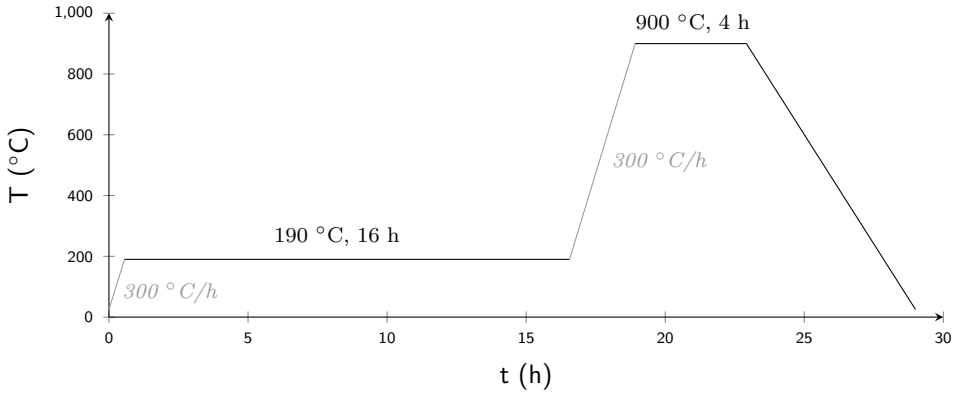

Figure 3.1: T-programme applied for calcination of powders, no distinct cooling rate

Step 3 - Homogenisation

Since the calcined powder was joined to a single clot, the sample was ground with an agate mortar before milling a second time with ethanol, according to the programme shown in Table 3.2.

Table 3.2: Settings for ball milling of the K-containing materials *after* the calcination process

parameter	**description**
speed [rpm]	300
time [min]	10
pause [min]	10
cycles [\#]	60
revers	off

Step 4 - Densification & Sintering

The powder was then dried and uni-axially pressed under a load of 5 tonnes for 2 minutes to obtain cylindrical pellets with diameters of 10/8 or 5 mm. The green bodies were then stacked and placed in a corundum crucible between two "protection" pellets to avoid Al-diffusion from the crucible into the samples. Additionally, the ground of the crucible was sprinkled with ZrO_2. Afterwards, the pellets were subjected to the sintering programme displayed in Figure 3.2.

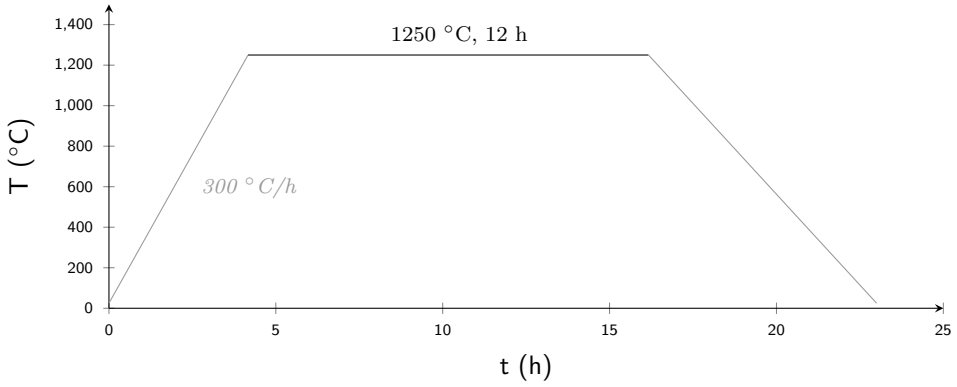

Figure 3.2: T-programme applied for calcination of powders, no distinct cooling rate

Step 5 - Surface Treatment

Prior to further preparations of the samples for PXRD (Powder X-Ray Diffraction), STA (Simultaneous Thermal Analysis), SEM (Scanning Electron Microscopy) and EIS (Electrochemical Impedance Spectroscopy) measurements, the surface regions of the pellets were removed by dry grinding and polishing, to achieve a flat surface and get rid of possible contaminations.

The following Figure 3.3 contains pictures that give a short insight into the different stages of the preparation process.

Figure 3.3: Stages of synthesis: ball milling (left), aggregation of powders after calcination (middle), pellets before sintering (right)

Adjustments of major synthesis route

Temperature programmes of calcination/sintering processes

Various measures were taken to improve the synthesis route and obtain best results concerning the phase-purity and microstructure of the K-based NaSICONs. For once, the calcination/sintering-temperatures and -times were varied, as summarised in the following Table 3.3.

Table 3.3: Alterations concerning the calcination (second holding stage)- & sintering-T/t for the preparation of the KZSP-pellets

calcination		*sintering*	
T [°C]	**t [h]**	**T [°C]**	**t [h]**
900	4	1250	12/20
850	4	1100	12
800	4/10	1000	12
750	4/10	950	12
		900	12

Educt amounts

Additionally, a test series was carried out, where different amounts of excess K_2CO_3 and $NH_4H_2PO_4$ were mixed to the starting composition to compensate for potential losses during the high annealing temperatures. The different approaches are listed down below (all data in wt-%):

- **5 %** K & **5 %** P
- **10 %** K& **10 %** P
- **5 %** K & **10 %** P
- **10 %** K & **5 %** P

Stoichiometry

In the end, also $KZr_2(PO_4)_3$ was synthesised according to the procedure explained in the Subsubsection "major route" with some slight alterations. Stoichiometric amounts of K_2CO_3, ZrO_2 and $NH_4H_2PO_4$ were weighed in and pellets pressed with a load of 5 tonnes for 1 to 2 minutes. As for this calcination step, the pellets were heated directly to 900 °C with a rate of 300 °C/h and 10 h-holding time.

Li-containing NaSICONs

The same way the K-based NaSICON compounds were synthesised, $Li_3Zr_2Si_2PO_{12}$ (Li_3ZSP), $Li_{3.4}Zr_2Si_{2.4}P_{0.6}O_{12}$ ($Li_{3.4}$ZSP) and $Li_{3.36}Zr_{1.96}Nb_{0.04}Si_{2.4}P_{0.6}O_{12}$ ($Li_{3.4}$ZSP (2%Nb)) were prepared. Again, stoichiometric amounts of the respective carbonate Li_2CO_3 were taken and mixed with ZrO_2, SiO_2, $NH_4H_2PO_4$ and Nb_2O_5.

Synthesis of NZSP

For later ion exchange experiments, in the end also $Na_{3.4}$ZSP was synthesised with the major solid state route applied to KZSP and LZSP.

3.3 Ion exchange

Besides solid state synthesis, different ion exchange experiments were conducted to prepare the wanted ceramics $K_{3.4}$ZSP, $Li_{3.4}$ZSP as well as $Ag_{3.4}Zr_2Si_{2.4}P_{0.6}O_{12}$ ($Ag_{3.4}$ZSP). The tests were carried out with calcined $Na_{3.4}$ZSP which was already available in our lab, as well as self-prepared sintered $Na_{3.4}$ZSP.

In the first approach, calcined NZSP-powder was stirred in 1 M $AgNO_3$-solution for 72 hours. Afterwards, the powder was washed several times with water and acetone before drying. To ensure maximum ion exchange, the 1M nitrate solutions were added in 2- to 3-fold stoichiometric excess.

In the second approach, sintered NZSP-powder was exchanged for 24 hours at 370 °C in the molten MNO_3-salts (M= Ag, K, Li; salts added in 20-fold weight excess to NZSP powder). Therefore, the sintered pellets were ground and additionally milled for several hours, since a smaller particle size should allow for a faster exchange. The respective settings can be found in Table 3.4.

Table 3.4: Settings for ball milling of $Na_{3.4}$ZSP

parameter	description
speed [rpm]	300
time [min]	10
pause [min]	10
cycles [#]	18
revers	off

3.4 Characterisation of the prepared solid state electrolytes

3.4.1 XRD analysis

All XRD-measurements were carried out with either a Rigaku MiniFlex or Bruker D8 Advance X-Ray Diffractometer with Bragg Brentano geometry and a Cu-Kα-radiation (λ= 1.5406 $\AA$). Samples were scanned in the region from 10° to 90° (2θ) with a step size of 0.01 ° and speed of 10 °/min. The Le Bail calculations for the different materials and stoichiometries were carried out by the supervisor.

3.4.2 Impedance measurements

Impedance measurements were performed on all sintered pellets, except for NZSP, using an Electrochemical Test Station POT/GAL coupled with an Alpha-A High Performance Frequency Analyser. To allow for conduction, the samples were sputtered with Au (K-based NaSICONs) or Pt ($Ag_{3.4}$ZSP). In addition, temperature-dependent measurements were carried out for KZP to spot potential phase changes.

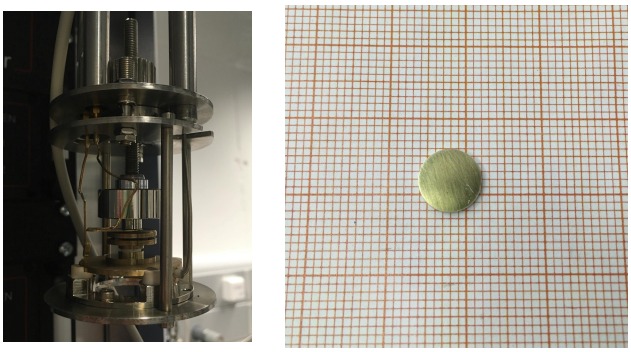

Figure 3.4: Pellet installed in the measuring station Novocontrol Concept 80 (left) and sample sputtered with Au (right)

3.4.3 STA + QMS measurements

Furthermore, thermal analysis was performed on sintered AZSP as well as un-calcined $K_{3.4}$ZSP powder to reveal underlying chemical processes taking place at higher temperatures. The measurements were done with a Simultaneous Thermal Analyser (4491 F1) from Netzsch, which was coupled to a Quadrupole Mass Spectrometer (403 C).

3.4.4 Cross sectioning and following SEM analysis

To take a look at the microstructure of the samples and also check the stoichiometric compositions, Scanning Electron Microscopy (SEM) measurements were carried out. Therefore, various pellets of KZSP and AZSP sintered at different temperatures were cut in half and embedded in a mixture of EpoFix Hardener and EpoFix Resin 15:2 (v/v) from Struers. After curing over night, the samples were sanded and polished. SEM analysis was done with a Zeiss Ultra Plus Field – Emission Scanning Electron Microscope (FE-SEM). The chemical compositions were determined by an Oxford Instruments X-MAX 50 mm^2 SDD Energy Dispersive X-Ray Spectrometry coupled to the SEM.

4 Results

4.1 KZSP

The main idea behind this master's thesis was the synthesis and characterisation of K-based NaSICON-materials with the generic formula being $K_{1+x}Zr_2Si_xP_{3-x}O_{12}$. Besides Hong and Goodenough, who have prepared $K_3Zr_2Si_2PO_{12}$ from $Na_3Zr_2Si_2PO_{12}$ by ion exchange in molten KNO_3,[21] no further characterisation of this stoichiometry has been carried out to our knowledge. Since not only the right composition and crystal structure are essential for ion conduction, but also the microstructure, solid state synthesis was attempted for K_3ZSP like carried out for NZSP in our lab. By altering the mechanical mixing processes and calcination/sintering temperatures, one can optimise the density of the pellets. Since $Na_{3.4}$ZSP (especially the one doped with 2 wt-% Nb), has shown higher ionic conductivities compared to other stoichiometries, a respective synthesis was carried out for $K_{3.4}$ZSP, as well as Nb-doped (2wt-%) $K_{3.4}$ZSP.

4.1.1 Visual Characterisation

In order to find the best annealing conditions for the K_3ZSP- and $K_{3.4}$ZSP/$K_{3.4}$ZSP (2%Nb)-pellets, the respective samples were subjected to different oven programmes as explained in the experimental section (see Section 3.2). The K_3ZSP-samples sintered above 1000 °C did show low mechanical strength and easily broke, which is why sintering was depressed to lower temperatures afterwards. Besides the sintering temperature, additionally the calcination conditions were varied (750 °C, 800 °C and 900 °C). The best results concerning the microstructure and porosity were obtained for the pellets calcined at 900 °C and sintered in the range of 900 °C to 1000 °C for 12 h as one can see in Figure 4.1 on the right-hand side. The samples calcined below, did show high degrees of deformation, porosity, slightly changed in colour and are therefore excluded in the following subsections.

Figure 4.1: Influence of the calcination temperature on the microstructure of the sintered pellets: 750 °C (left); 800 °C (middle); 900 °C (right)

4.1.2 XRD analysis

The following Figure 4.2 shows a selection of obtained XRD patterns of K_3ZSP (left-hand side) and $K_{3.4}ZSP$/$K_{3.4}ZSP$ (2%Nb) (right-hand side), treated at different sintering temperatures. Pellets of K_3ZSP were annealed at 900, 1000, 1100 and 1250 °C for 12 h, the ones of $K_{3.4}ZSP$ and $K_{3.4}ZSP$ (2%Nb) at 900 and 1000 °C for 12 h, respectively.

As one can see, the width of the respective reflexes and therefore the degree of crystallinity for the samples, increases slightly with increasing temperature for both stoichiometries. Despite minor intensity shifts as can for example be seen for the second most prominent reflex, doping of $K_{3.4}ZSP$ with 2 wt-% Nb, does not lead to an alteration of the obtained pattern.

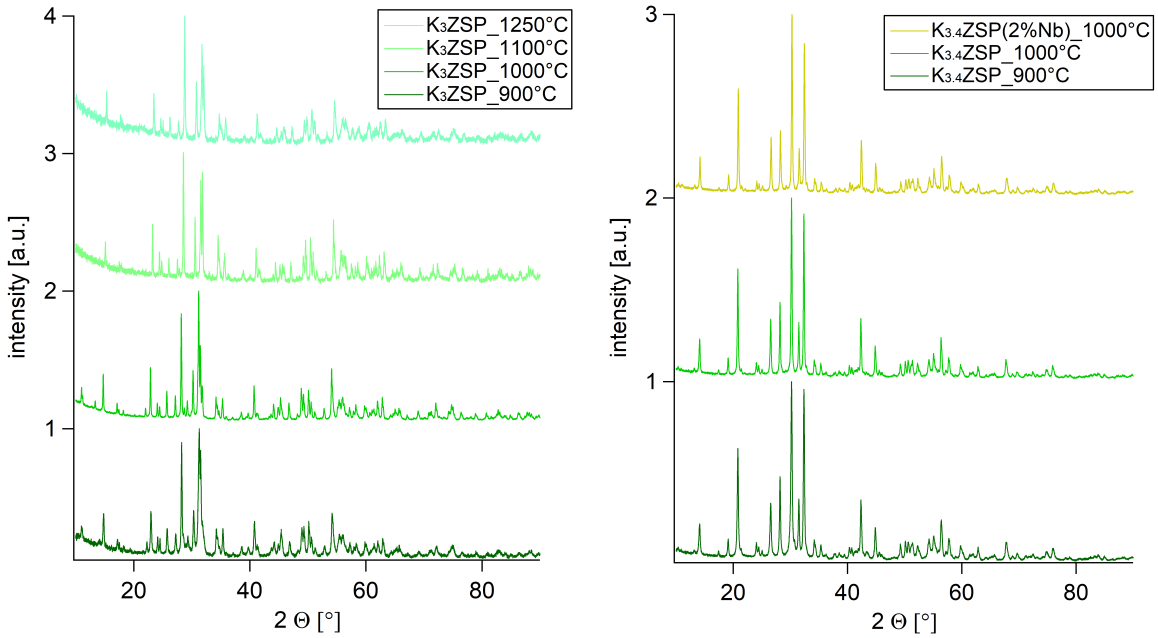

Figure 4.2: Influence of the sintering temperature on the measured XRD patterns of K_3ZSP (left) and $K_{3.4}ZSP$ (right)

Figures 4.3 and 4.4 present the Le Bail fits for K_3ZSP and $K_{3.4}ZSP$ treated at 1000 °C. For both stoichiometries, the best fit could be obtained with the monoclinic crystal structure $P2_1/c$. The difference between the observed intensities (light-green dots) and the calculated ones (dark-green lines) was plotted beneath the pattern (black lines), to demonstrate the respective accuracy or deviation from the calculations. Additionally, contributions from un-reacted starting materials like ZrO_2 (dark-orange) and SiO_2 (light-orange) were considered during the fitting process. The reflexes which could be assigned to the NaSICON-phase were marked in dark-green.

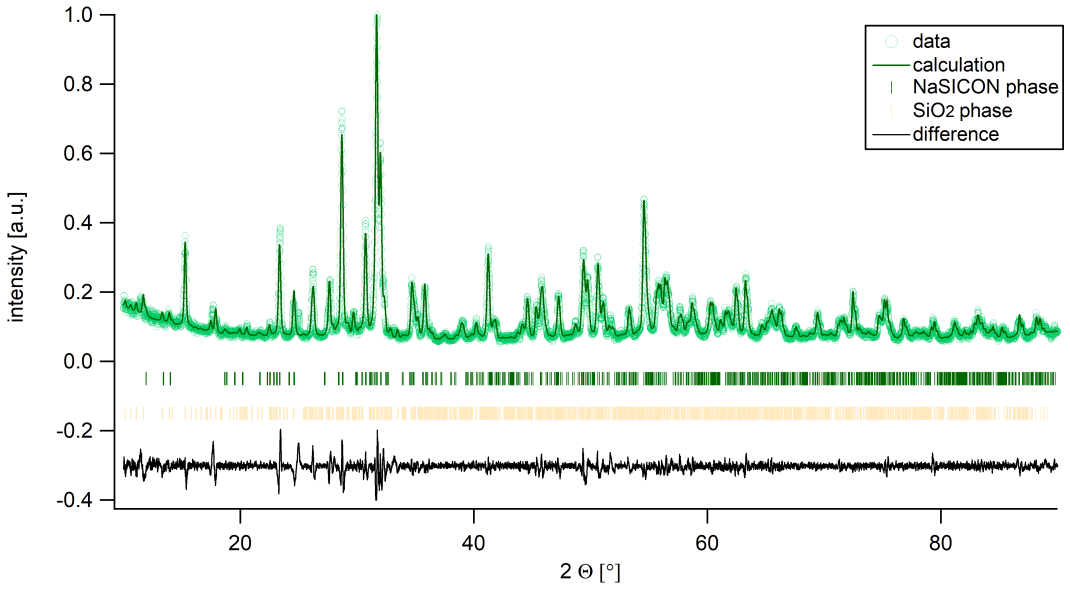

Figure 4.3: XRD pattern of K_3ZSP at 1000 °C with proposed fit

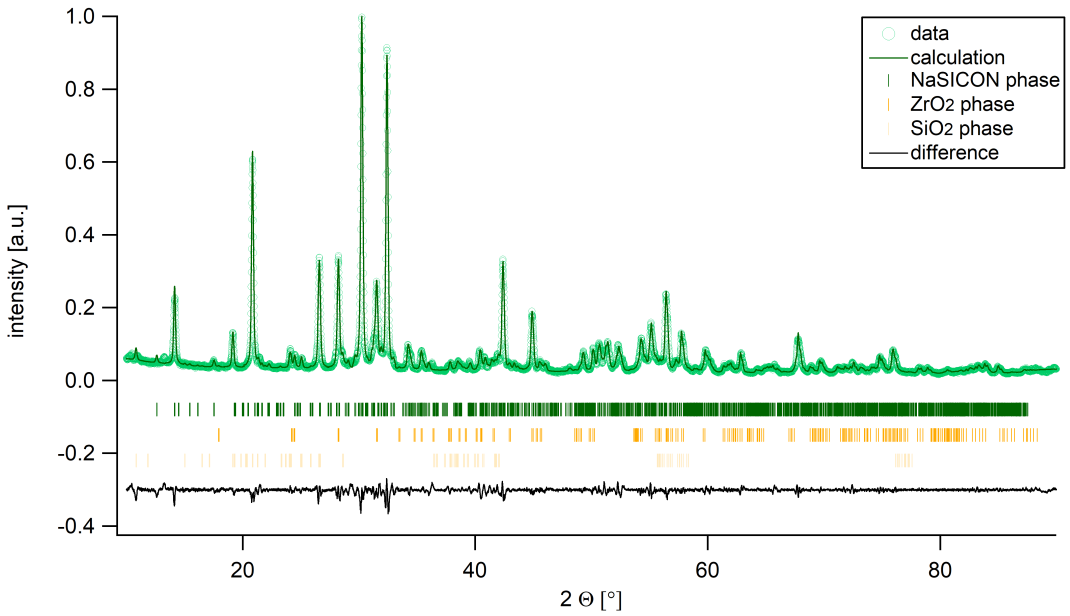

Figure 4.4: XRD pattern of $K_{3.4}ZSP$ at 1000 °C with proposed fit

Since the obtained patterns show a high amount of reflexes and no structure models are available for these materials, it is difficult to assign the respective reflexes and determine a distinct space group. Besides, the synthesis of phase-pure NaSICON-type materials has already been proven difficult in the past,[66] which can most of the times be traced back to the evaporation of Na and P during the heat-treatments of the synthesis. This loss results in an excess of ZrO_2, which in turn segregates at the grain boundaries and therefore hinders ionic conduction within the material as well as close contact between the particles.[19] Ladenstein *et al.*[67] showed, that

depending on the stoichiometry as well as crystallinity of such NaSICONs (here $Na_3Sc_2(PO_4)_3$) and their synthesis route, the amounts of losses are varying as one can deduce from Figure 4.5 on the left. Additionally, the temperature of the corresponding order-disorder phase transitions are shifting like shown in the respective DSC measurements on the right.

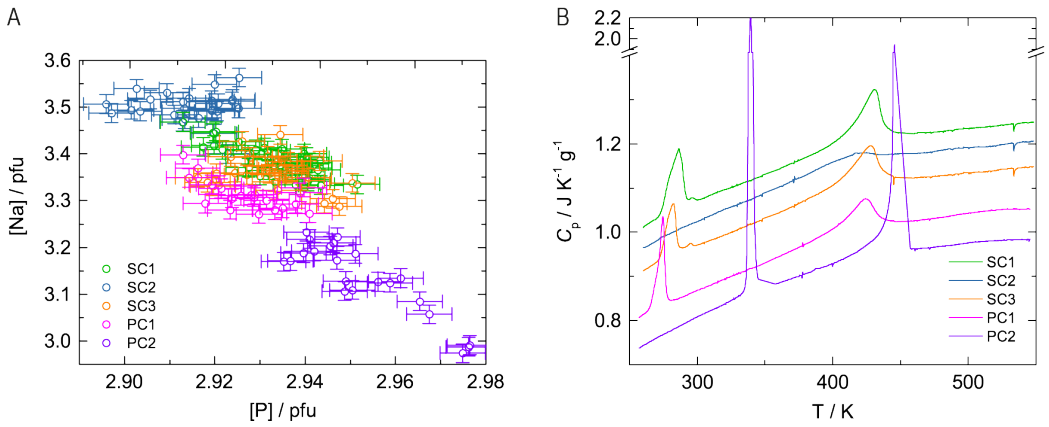

Figure 4.5: Observed loss of Na and P in $Na_3Sc_2(PO_4)_3$ for single crystals and polycrystalline material (a) with respective DSC measurements (b); attempts of synthesising the same material with same starting mixtures but different synthesis routes[67]

Ruan *et al.*[19] recently could manage to synthesise Na_3ZSP without any ZrO_2-side phase by carrying out the respective solid state synthesis with excess Na_2CO_3 and $NH_4H_2PO_4$ in order to counterbalance Na and P losses during calcination. Therefore, excess K_2CO_3 and $NH_4H_2PO_4$ (5 and 10 wt-%, respectively) were added to the stoichiometric mixtures to compensate for such possible losses. The corresponding XRD patterns are displayed in Figure 4.6. Unfortunately, these adaptions did not yield phase-pure samples and barely any differences can be found between the displayed patterns.

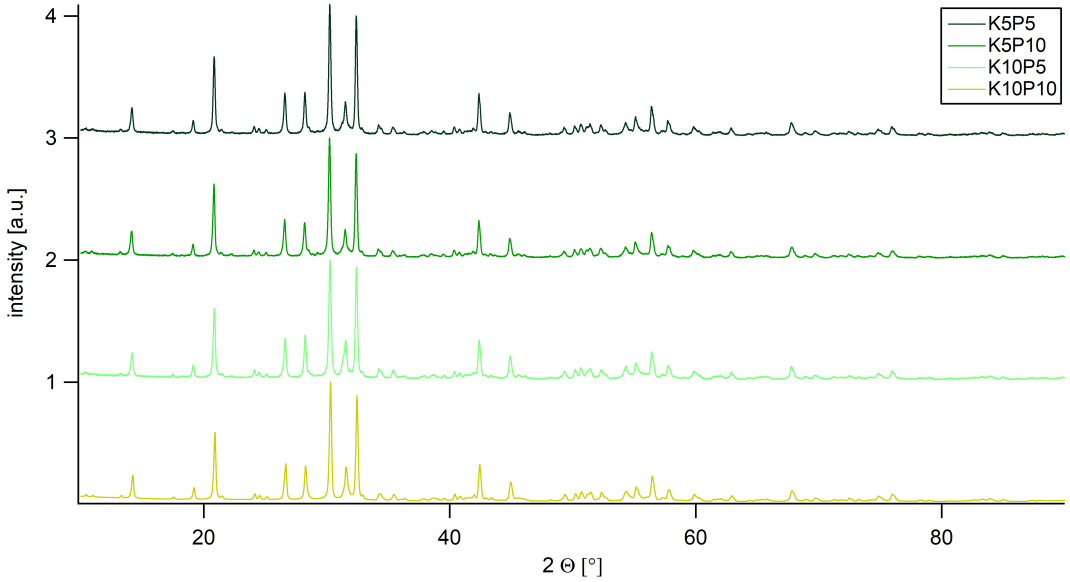

Figure 4.6: XRD patterns for $K_{3.4}$ZSP-samples with excess K and P

4.1.3 STA measurement

Since none of the implemented synthesis strategies did yield phase-pure products, an STA (=Simultaneous Thermal Analysis) measurement of the un-reacted starting mixture for the $K_{3.4}$ZSP-synthesis was carried out to reveal underlying chemical and physical processes at temperatures up to 1000 °C. By combining the information output from the DTA and TGA curve with MS (= Mass Spectrometry), an even better insight into the corresponding reactions can be gained. The respective curves are shown in Figure 4.7.

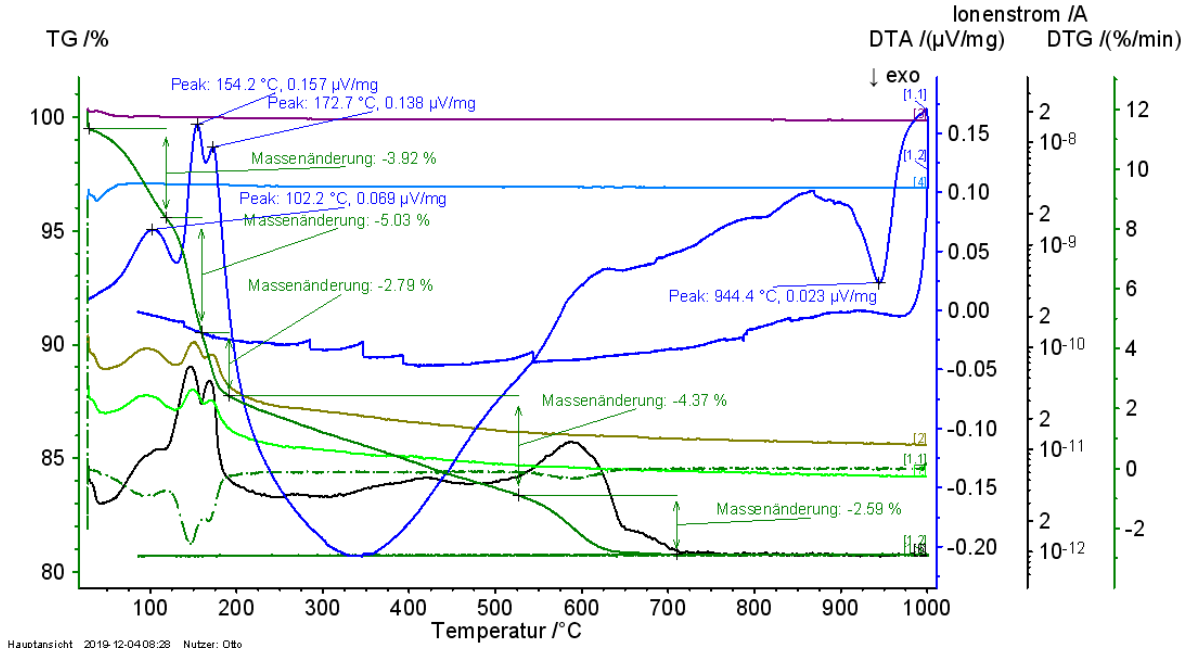

Figure 4.7: STA analysis of the starting mixture for the $K_{3.4}$ZSP-synthesis

The dark-green curve represents the TGA-curve, whereas the dark-blue one displays the results from the DTA measurement. The dashed line stands for the deviation DTG, given in %/min, and demonstrates that mass loss takes place in several steps. First losses can be observed at 102.2 °C, 154.2 °C and 172.7 °C, as a result of three endothermic processes. Since the preparation of the KZSP-samples was not carried out under inert atmosphere, the first peak at 102.2 °C possibly results from the loss of water. The other two peaks most presumably can be assigned to the loss of NH_3 and NH_4^+, since $NH_4H_2PO_4$ decomposes at such temperatures.[68] This is also the reason, why the calcination programme chosen exhibits an additional step at 190 °C for 16 hours, before heating up to e.g. 900 °C. Since both, NH_3 and OH^-, as well as NH_4^+ and H_2O show almost identical masses, a complete differentiation is not possible. However, the mass losses obtained *via* MS being 17 (light-green) and 18 (dark-green), confirm the evaporation of such compounds.

As the temperature is increased, again a mass loss of 44 can be observed which could be assigned to a decarbonisation reaction. At 944.4 °C, another exothermic reaction takes place. Since no mass losses were recorded, these may result from e.g. phase transitions or crystallisation processes. From the cooling curve one can deduce, that the observed events are not reversible (kinks in curve are just artefacts).

4.1.4 SEM analysis

To allow for further investigations concerning the microstructure and chemical composition of the KZSP-pellets, SEM analysis was carried out for K_3ZSP, $K_{3.4}ZSP$ and $K_{3.4}ZSP$ (2%Nb).

The preparation of the K_3ZSP-cross-sections was quite challenging, since the size of the particles is in the nm-range like can be seen in Figures 4.8 and 4.9. The interior of the samples sintered at 1000 °C seems to exhibit a higher degree of porosity compared to the outer regions, whereas in the samples annealed at higher temperatures (here 1100 °C) no evidence of similar occurrences could be detected. However, as already mentioned in Section 4.1.1, the samples sintered at 1100 °C were prone to breakage. A fact, that can most presumably be traced back to the appearance of micro-sized cracks, also visible in Figure 4.9 on the left-hand side.

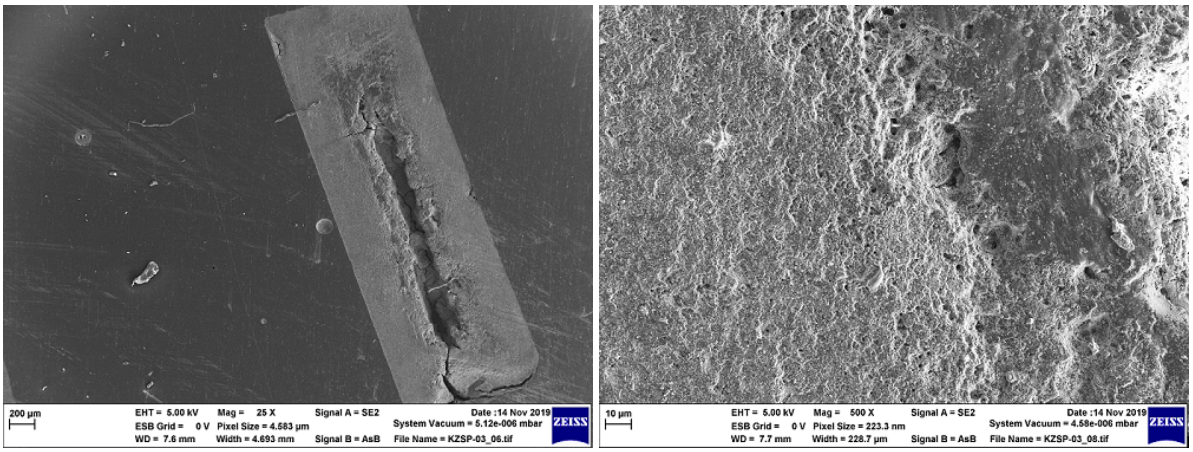

Figure 4.8: Analysis of the cross-section of K_3ZSP 1000 °C

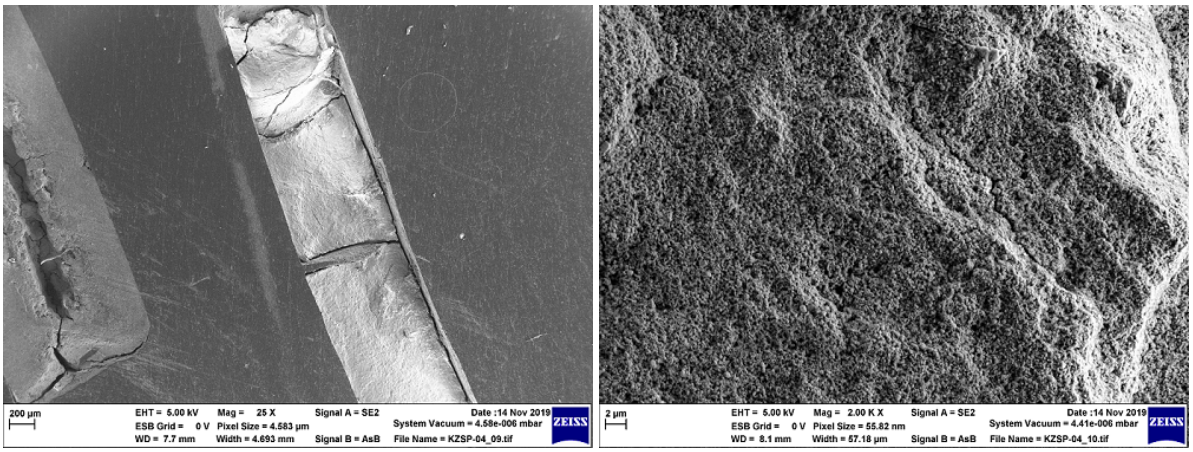

Figure 4.9: Analysis of the cross-section of K_3ZSP 1100 °C

Table 4.1 gives an overview of three Energy-Dispersive X-Ray Spectroscopy (EDX) spectra, obtained from different regions of the K_3ZSP-pellet sintered at 1000 °C. For comparison, the theoretical amounts present in this stoichiometry are additionally displayed. Besides K, all other elements included in the NaSICON-framework match with the calculated values when

considering the significant deviations induced by spectrum 2, which could also indicate a possible side phase. A picture of the analysed regions can be found in the appendix (8.1).

Table 4.1: EDX measurements of K_3ZSP annealed at 1000 °C

	amount [wt-%]						
Spectrum	**O**	**Na**	**Si**	**P**	**K**	**Zr**	**Total**
1	32.33	0.14	11.26	5.1	13.06	38.11	100
2	41.16	0.16	14.29	6.09	12.26	26.03	100
3	33	0.17	9.02	6.16	12.91	38.75	100
Mean	**35.49**	**0.16**	**11.52**	**5.78**	**12.75**	**34.3**	**100**
Std. dev.	*4.92*	*0.01*	*2.65*	*0.59*	*0.43*	*7.16*	
K_3ZSP	**33.17**	**0**	**9.7**	**5.35**	**20.26**	**31.52**	**100**

The $K_{3.4}ZSP$ and $K_{3.4}ZSP$ (2%Nb) pellets did show similar behaviour to the K_3ZSP-samples. Again, highly porous networks as well as further inhomogeneities concerning the microstructure could be observed. For the pellet annealed at 950 °C, additionally areas with as it seems segregations could be found as shown in Figure 4.10 on the right-hand side.

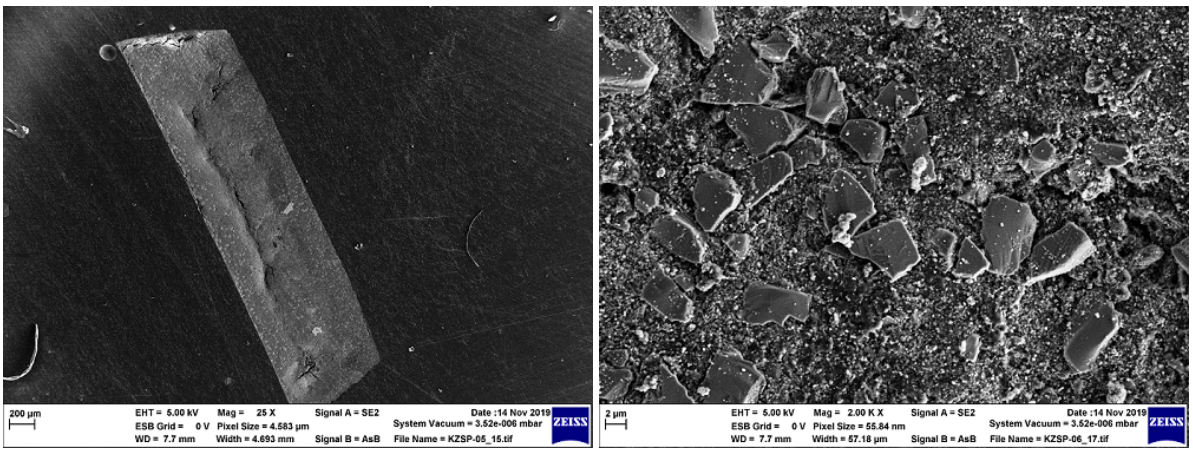

Figure 4.10: Analysis of the cross-section of $K_{3.4}ZSP$ 950 °C

The different regions analysed can be found in Table 4.2 (related picture 8.1 again displayed in the appendix). The green data set is the one that matches best with the calculated contributions for this stoichiometry. The values highlighted in light-orange were obtained from analysis of the already mentioned depositions shown in Figure 4.10. As one can see, they consist almost entirely of Si. Spectrum one (dark-orange) displays the elemental composition obtained for a region that seems to be rich in silicone oxide.

Table 4.2: EDX measurements of $K_{3.4}ZSP$ annealed at 950 °C

			amount [wt-%]			
Spectrum	**O**	**Si**	**P**	**K**	**Zr**	**Total**
2	57.26	36.77	0.71	2.87	2.4	100
2	46.73	13.69	2.77	12.45	24.36	100
3	35.77	14.74	2.97	17.23	29.29	100
4	2.26	97.53	0	0.2	0	100
5	2.55	96.38	0	0.27	0.8	100
6	39.21	15.38	2.23	13.08	30.1	100
$K_{3.4}ZSP$	**32.36**	**11.36**	**3.13**	**22.4**	**30.75**	**100**

These EDX spectra clearly show that neither K_3ZSP nor $K_{3.4}ZSP$ could be synthesised phase-pure with the proposed solid state synthesis methods. By taking a look at all of the obtained elemental compositions (except for the areas rich in Si), it becomes evident that all of these regions are poor in K. When considering the size difference of a K-ion and Na-ion, it seems highly likely, that due to the substitution of P with Si, the polyhedra in the crystal structure are too small to accommodate such a high amount of K-ions within the NaSICON-structure. This fact could also explain the fluctuations of the elemental compositions obtained for the different spectra.

4.2 KZP

Since the crystal lattices of K_3ZSP and $K_{3.4}ZSP$ seem to be too small for the K-ion to fit in, the material composition was revised and a new approach was developed where the relatively small Si-ion is completely removed from the composition. Afterwards, it is possible to replace the Zr-ion with larger ions (e.g. La) and therefore open up the crystal lattice. Before carrying out a test series with various different substitutions, the "parent compound" which lacks any of these substituting elements, $KZr_2(PO_4)_3$ (KZP), has to be synthesised and characterised first. This compound has already appeared in some earlier reports[21,69,70,71,72,73] and was prepared according to the major synthesis route mentioned in Section 3.2 with some slight adaptions of the calcination process integrated from the synthesis of $LiZr_2(PO_4)_3$.[44]

4.2.1 Visual Characterisation

The following Figure 4.11 shows images of KZP-pellets annealed at 1250 °C for 12 h. It can be stated, that a longer pressing time of 2 min instead of 1 min leads to samples with reduced porosity as a result of improved contact between the particles.

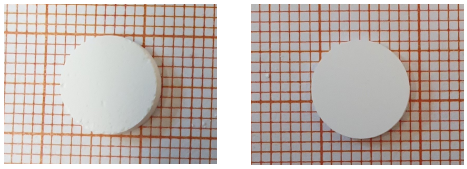

Figure 4.11: Pellets of KZP pressed for 1 min (left) and 2 min (right), both sintered at 1250 °C

4.2.2 XRD analysis

Figure 4.12 displays the XRD patterns of the calcined (light-green) and sintered (dark-green) powder in comparison to a reference plot (black) taken from ICSD (# 4427), which exhibits the rhombohedral crystal structure $R\text{-}3c$.

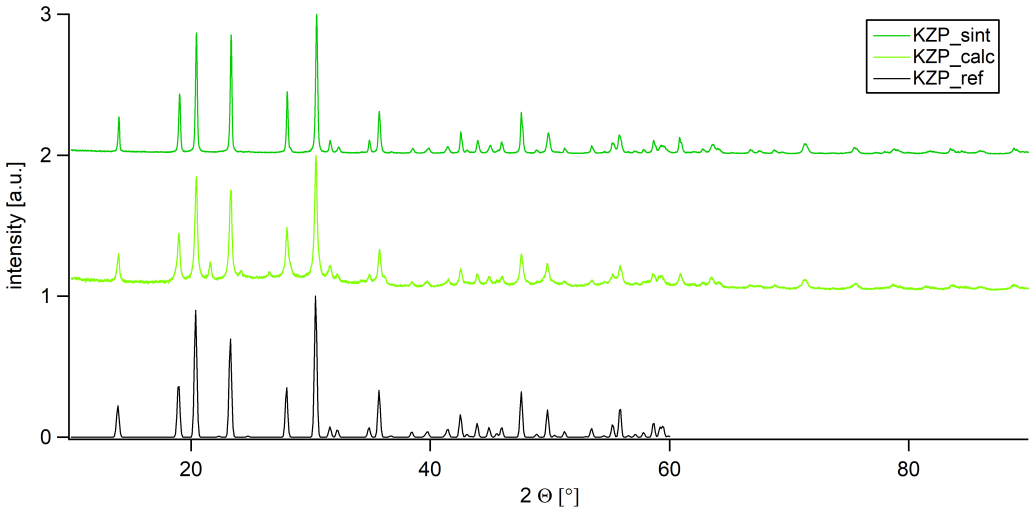

Figure 4.12: XRD patterns of calcined and sintered KZP in comparison to ICSD # 4427

As one can see, the reflexes of the sintered sample match with the ones from reference and no additional contributions from side phases can be detected. It can be assumed, that the powder synthesised is entirely phase-pure. Like mentioned in Subsection 1.3.2, the highest ionic conductivities in the case of NaSICON-type materials could be obtained for compositions crystallising in a rhombohedral crystal structure, which is why this space group is highly desirable.

4.2.3 Electrical studies

As the material synthesised was phase-pure, one of the sintered pellets was sputtered with Au on two opposing sides and the dielectric properties analysed *via* EIS. To identify any possible phase transformations, the measurements were carried out in a total temperature range from -100 °C to 230 °C. Since Yamanaka *et al.*[73] reported an unusual conductivity/temperature dependence for KZP when measured in atmosphere, the tests were usually carried out in N_2. Only in the first measurement series, which is depicted in Figure 4.13, the impact of the atmosphere (run1) in comparison to N_2-flow (run2) was determined. In the middle of the second run, the sample was again removed from the measuring chamber and the conductivity immediately increased again, showing, that moisture has a significant impact on the measured conductivity.

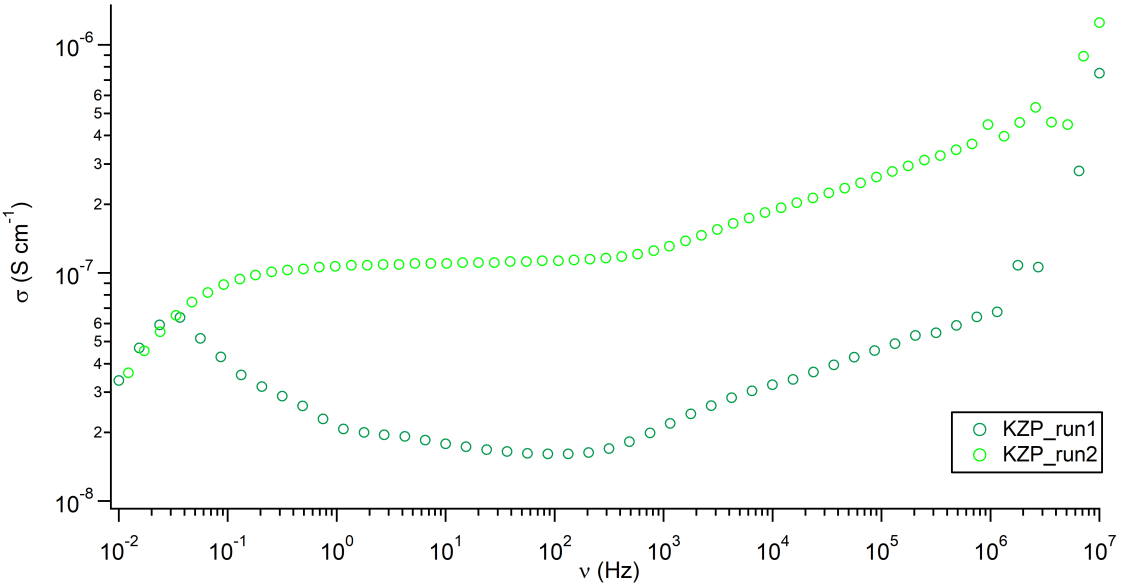

Figure 4.13: Conductivity isotherms for KZP-pellet measured at atmosphere (run1) and under N_2-flow (run2) at RT

For the second measurement series, the pellet was first cooled down from 20 °C to -100 °C and successively increased by 20 °C to 220 °C. Afterwards, the sample was again cooled down in 20 °C-steps to RT. A selection of the isotherms obtained from the last cooling step can be found in Figure 4.14. As a consequence of the heating steps prior, the sample should be completely stripped of any moisture. The data measured at temperatures lower than 20 °C is not shown, since the conductivity was too low for the device to properly display it.

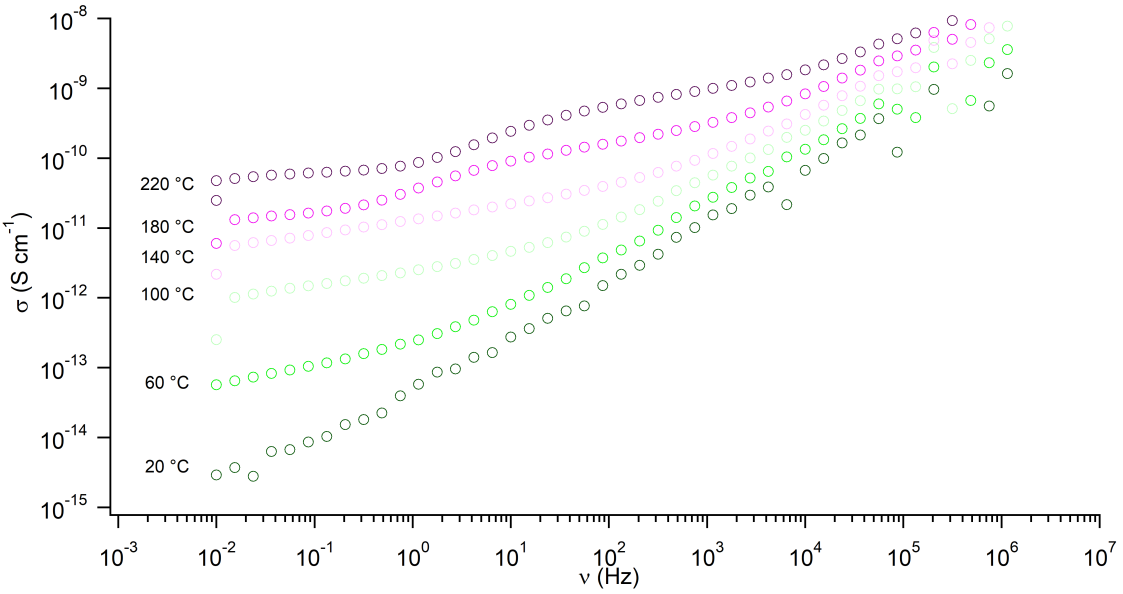

Figure 4.14: Conductivity isotherms for KZP-pellet measured in N_2-atmosphere from 20 to 220 °C

At higher temperatures two distinct plateaus can be differentiated, which are shifted to lower frequency values as the temperature decreases. Those can be associated with the bulk and grain boundary contributions of the sample. At RT, none of the two are visible anymore. Therefore, a third measurement series was carried out and this time, the pellet was first dried at 100 °C, before starting the measurement at 0 °C and going up to 230 °C. Overall, a step size of 10 °C was chosen. Only in the intervals ranging from 0 °C to 80 °C and 160 °C to 230 °C, it was reduced to 5 °C to obtain more data points in these regions and spot potential phase changes.

As it was still difficult to detect the plateaus of the different contributions, especially at low temperatures, the respective conductivities were accessed by visualising the impedance data in form of Nyquist plots. By plotting the negative values of the imaginary part against the real part of the impedance, a complex plane in the form of several semicircles is obtained (see Figure 4.15).

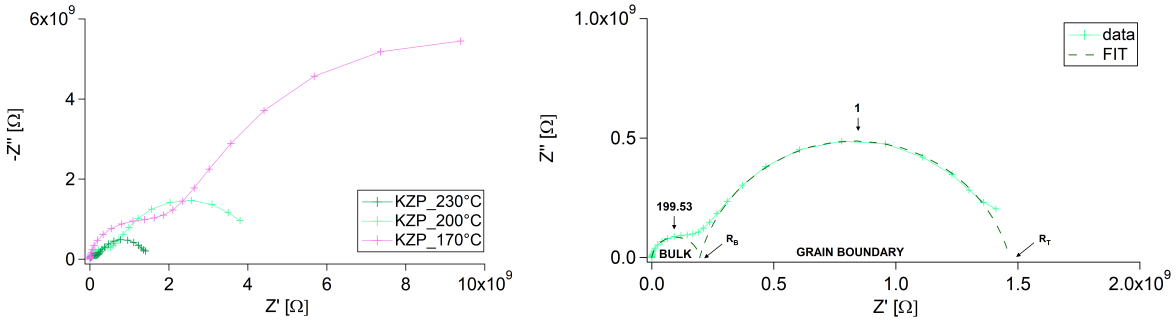

Figure 4.15: Visualisation of (a) Nyquist plots obtained at different temperatures ranging from 170 °C to 230 °C (b) how the respective data (here at 230 °C) was fitted

The one at higher frequencies represents the bulk process, whereas the second one at lower frequencies shows the grain boundary contribution.[54,74] By fitting these semicircles, the corresponding resistances, which are given by the intersections of the curves with the x-axes, can be retrieved. The best results could be obtained for the 230 °C-measurement (see Figure 4.15 on the left-hand side). Here, the resistances of the bulk and grain boundary process amount to 1.82E+08 Ω (C=8.46E-11 F/cm) and 1.33E+09 Ω (C=1.24E-10 F/cm) respectively, giving a total resistance of 1.51E+09 Ω. As one can deduce from the left image, the resistances of the respective processes decrease with increasing temperature.

When applying the following relation shown in equation 4.1, the conductivities at the different temperatures can be accessed:

$$\sigma' = \frac{1}{Z'} \cdot \frac{l}{A} \tag{4.1}$$

where l stands for the thickness of the pellet and A for the surface contacted. For the 230 °C-measurement, the total conductivity amounts to 2.04E-10 S/cm.

When considering equation 2.23 displayed in Subsection 2.5.2, it is possible to access the activation energies of the corresponding contributions by visualising the obtained data in form of an Arrhenius plot as shown in Figure 4.16. The markers represent the calculated conductivities, plotted in a logarithmic manner against a reciprocal value of the temperature. This way, a straight line can be fitted through the points and the activation energy calculated from the slope. Since the semicircle for the grain boundary and bulk process vanish at 155 °C and 60 °C, respectively, only the upper temperature segments could be used for the calculations of the activation energies.

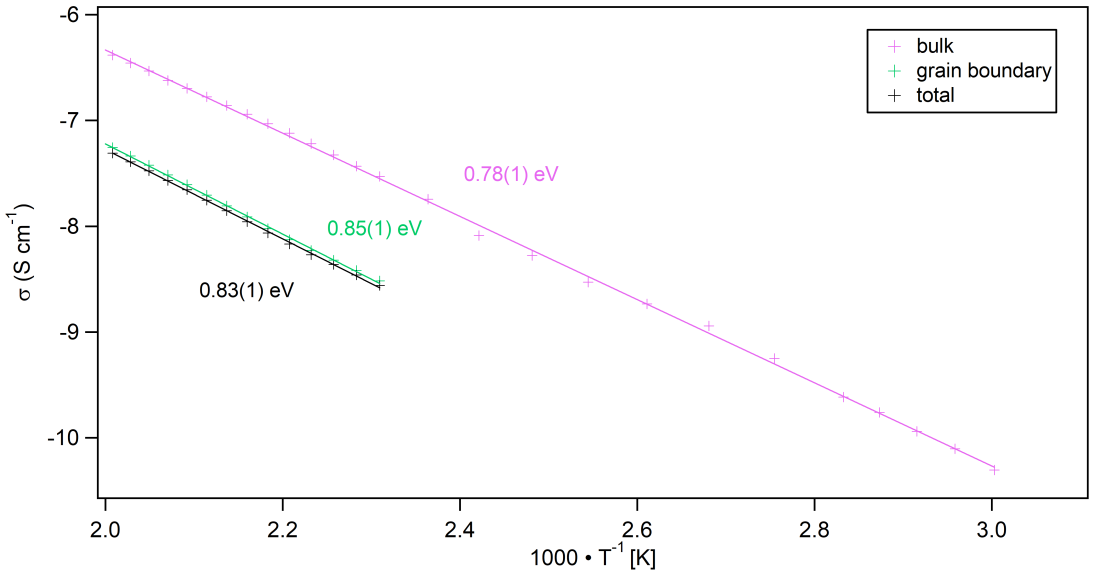

Figure 4.16: Arrhenius plot for KZP created from measurements ranging from 230 °C to 60 °C

For the bulk contribution, the activation energy of the ion hopping process amounts to 0.78(1) 1 eV, whereas for the grain boundary this values is slightly higher, being 0.85(1) eV. In total, an activation energy of 0.83(1) eV ($\hat{=}$ 80.1 kJ/mol) can be derived, which correlates well with literature (72.5 kJ/mol).[72] Since all of the processes exhibit a linear regression, it can be assumed that the material does not undergo any phase changes within the analysed temperature region. This observation is consistent with assumptions, as the crystal structure of the compound already exhibits the highest symmetry.

4.3 AZSP

To prepare the Ag-based analogue of $Na_{3.4}Zr_2Si_{2.4}P_{0.6}O_{12}$, the Na-ions of this compound (which was already available in our lab) were exchanged by Ag via stirring in a 1 M $AgNO_3$-solution for three days. Hong and Goodenough have shown in one of their initial reports, that Ag_3ZSP can be synthesised by ion exchange in melt for four hours. Since Sadaoka *et al.*[75] struggled with low mechanical stability and significant porosity of their Ag_3ZSP-pellets prepared from the sintered Na-analogue, calcined powder was used for this synthesis.

4.3.1 Visual Characterisation

After ion exchange in $AgNO_3$-solution for 72 hours, the initially white powder turned brown as one can see in the pictures displayed in Figure 4.17. The pellets sintered at temperatures below 800 °C did also exhibit a brown/grey colour, whereas above, the samples got more and more white/light-grey as the temperature was increased. Some of them even showed a metallic lustre at the surface, which could indicate a deposition of metallic Ag.

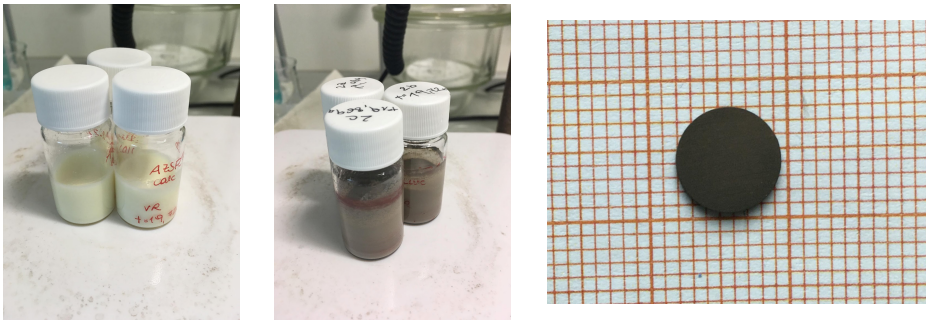

Figure 4.17: Change in colour during AZSP-synthesis at t=0 h (left) and t=72 h (middle) and pellet sintered at 600 °C (right)

4.3.2 XRD analysis

Figure 4.18 displays all XRD patterns gained by sintering $Ag_{3.4}ZSP$ in a temperature range of 600 °C to 1250 °C. The crystal sizes of the powders obtained after 600 and 700 °C are pretty small, leading to a broadening of the observed reflexes. At temperatures above 900 °C, the pattern completely changes, resulting either from a phase change or a degradation of the material, which has also been reported for Ag_3ZSP in that approximate temperature range.[75]

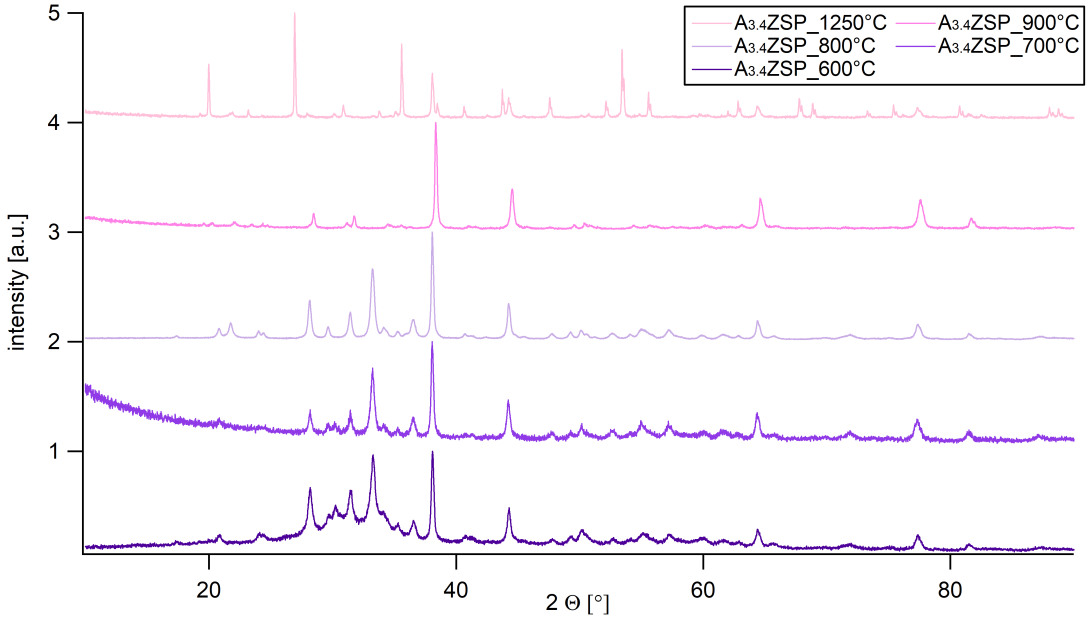

Figure 4.18: Influence of the sintering temperature on the measured XRD patterns of $Ag_{3.4}ZSP$

A proposed Le Bail fit for the sample sintered at 800 °C can be found in Figure 4.19. The best match could be obtained with the monoclinic space group $C2/c$. However, the difference between the experimentally obtained data and the calculations, plotted in black, shows that at least one additional side phase is present.

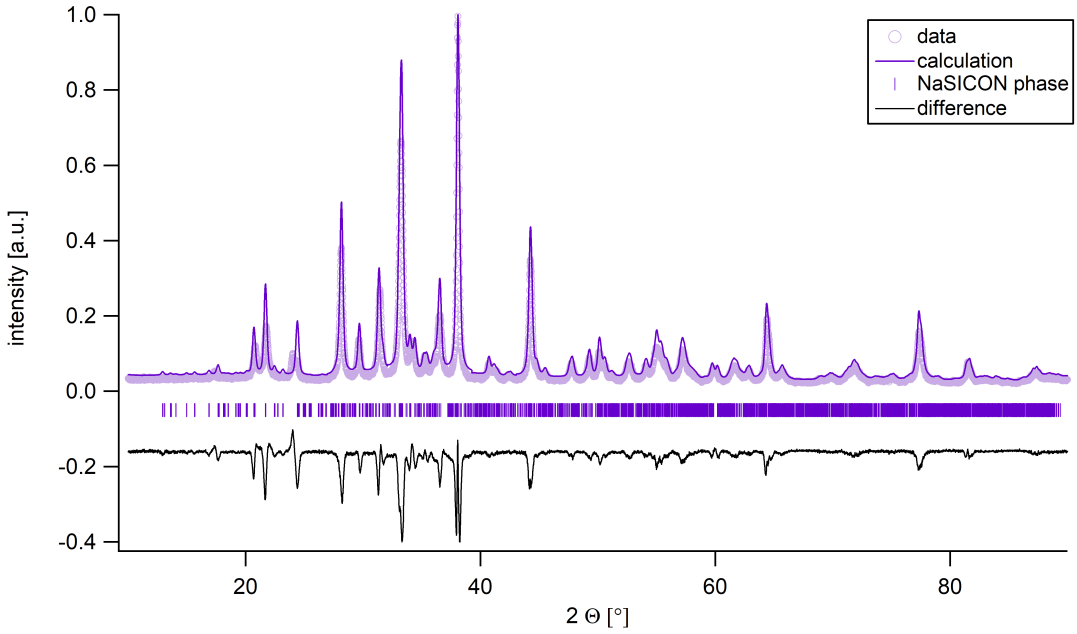

Figure 4.19: XRD patterns of $Ag_{3.4}ZSP$ with proposed fit

4.3.3 STA measurement

Also for AZSP, STA measurements were carried out from room temperature up to 1000 °C to analyse its chemical stability during sintering. Like in the case of $K_{3.4}$ZSP, the outcome of DTA (dark-blue) and TGA (dark-green) analysis are plotted together with mass losses obtained from MS.

The first peak that appears at 126.9 °C may again result from the loss of water. Shortly after, a small contribution with a mass of 44 can be observed, that again appears at ca. 500 °C. Several smaller exothermic events can be seen starting at around 600 °C, with one shoulder at ca. 740 °C that seems to represent a reversible process. These exothermic signals most presumably result from decomposition/oxidation sequences taking place in the material. However, since the measurement was carried out in O_2-atmosphere, no precise examination of the peaks can be done. Sadaoka *et al.*[75] reported the formation of $ZrSiO_4$-phases and deposition of metallic silver for Ag_3ZSP fired above 700 °C which could be described by some of these exothermic signals.

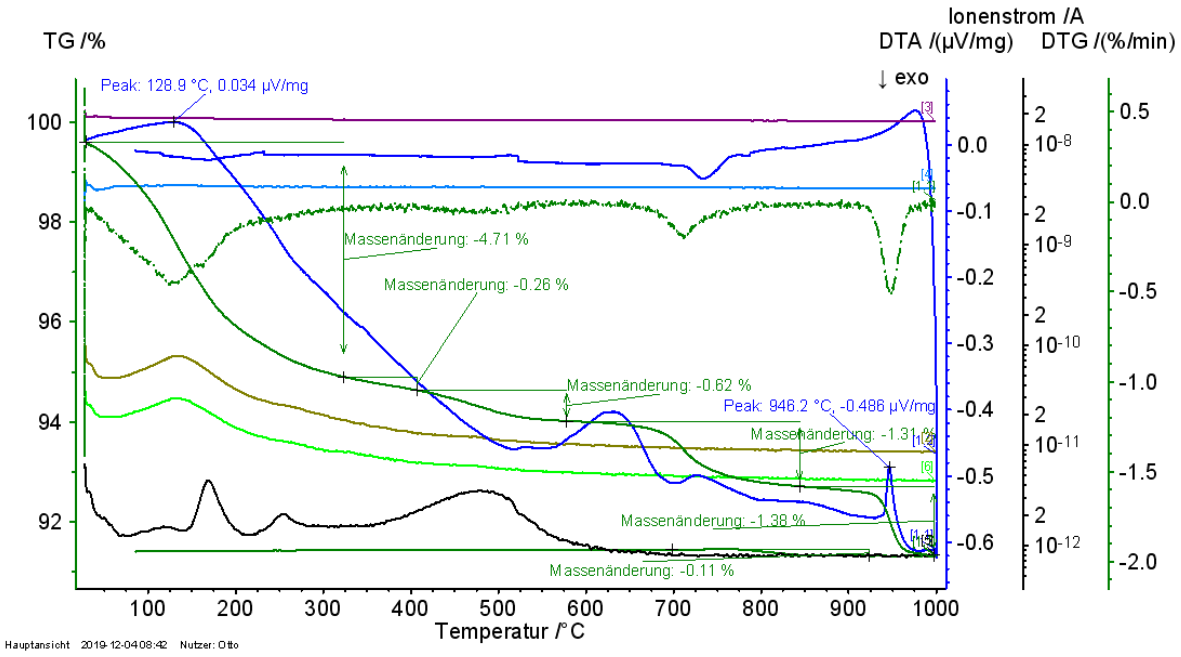

Figure 4.20: STA analysis of $Ag_{3.4}$ZSP obtained by ion exchange from $Na_{3.4}$ZSP

4.3.4 SEM analysis

To confirm the interpretation of the STA measurement, SEM analysis was carried out for $Ag_{3.4}$ZSP-pellets annealed at 600, 800 and 1100 °C. Figure 4.21 shows some close-up pictures of the cross-section from the 600 °C-pellet. It is evident, that the microstructure is not completely uniform, which can most presumably be traced back to a small amount of phase-impurities within the $Na_{3.4}$ZSP-batch used for the preparation of this specific sample.

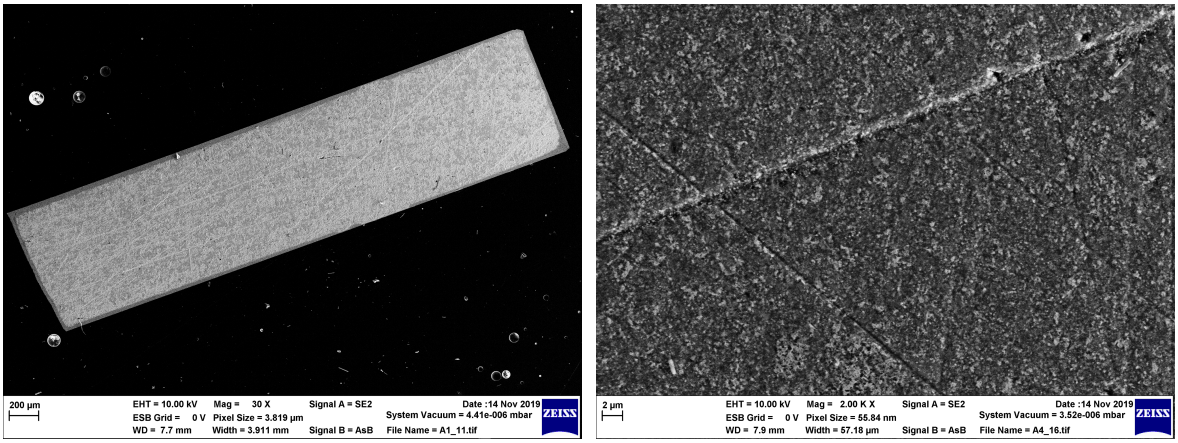

Figure 4.21: Cross-section of $Ag_{3.4}ZSP$ sintered at 600 °C (left) and 700 °C

Table 4.3 displays the results of the associated EDX measurements carried out at two distinct positions (respective regions are once more displayed in the appendix in Figures 8.2 and 8.3). Since only two data sets are available from this sample, the mean value and standard deviation have to be regarded with a certain precariousness. As one can see, Na could be successfully exchanged by Ag with a percentage near 100. The discrepancy between the calculated and observed values for this stoichiometry are most presumably caused by the already mentioned phase-impurities.

Table 4.3: EDX measurements of $Ag_{3.4}ZSP$ annealed at 600 °C

	amount [wt-%]						
Spectrum	**O**	**Na**	**Si**	**P**	**Zr**	**Ag**	**Total**
1	27.96	0.65	7.88	1.59	24.09	37.83	100
2	30.17	0.4	7.92	1.41	19.38	40.72	100
Mean	**29.07**	**0.52**	**7.9**	**1.5**	**21.74**	**39.27**	**100**
Std. dev.	*1.56*	*0.17*	*0.03*	*0.12*	*3.33*	*2.04*	
Ag3.4ZSP	**23.21**	**0**	**8.15**	**2.25**	**22.06**	**44.34**	**100**

In comparison to the pellets sintered at 600 and 700 °C, new light depositions could be found in the cross-sections of the pellets treated at 800 °C (see Figure 4.22). This second phase or decomposition product was observed to be almost homogeneously distributed throughout the whole pellet.

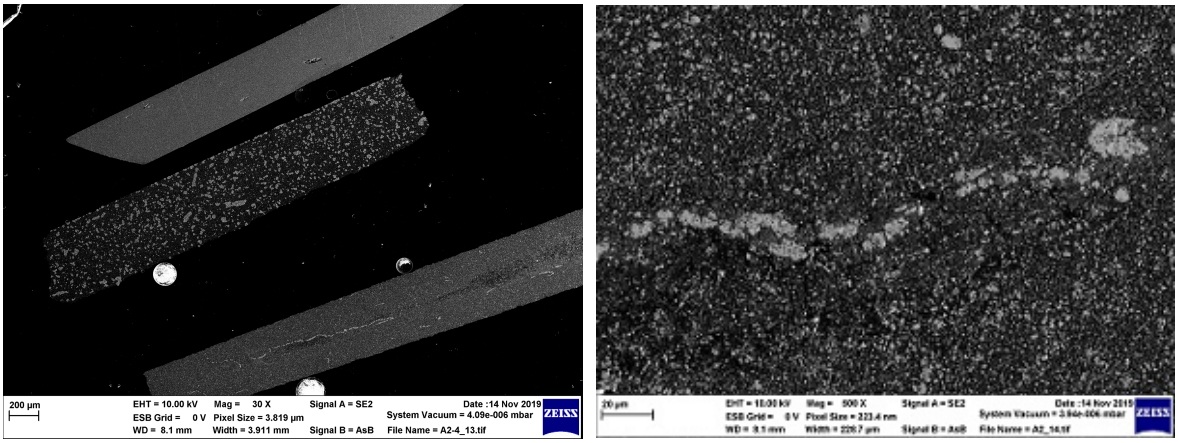

Figure 4.22: Cross-section of $Ag_{3.4}$ZSP sintered at 800 °C

EDX measurements of these areas, which are displayed in Table 4.4, could reveal, that Ag-rich regions have developed at this temperature.

Table 4.4: EDX measurements of $Ag_{3.4}$ZSP annealed at 800 °C

	amount [wt-%]						
Spectrum	**O**	**Na**	**Si**	**P**	**Zr**	**Ag**	**Total**
1	13.22	0	4.02	0.72	8.31	73.73	100
2	18.07	0	5.37	1.18	13.78	61.6	100
3	29.93	0	14.69	1.2	22.74	31.43	100
Ag3.4ZSP	**23.21**	**0**	**8.15**	**2.25**	**22.06**	**44.34**	**100**

Figure 4.23 shows, how the microstructure changes with further increasing the sintering temperature (from 900 °C up to 1100 °C). Again, the elemental composition was analysed for different microstructural features in the 1100 °C-pellet and the obtained results are displayed in Table 4.5. The spectra reveal, that metallic Ag (violet), as well as phases consistent with $ZrSiO_4$ (orange) are present.

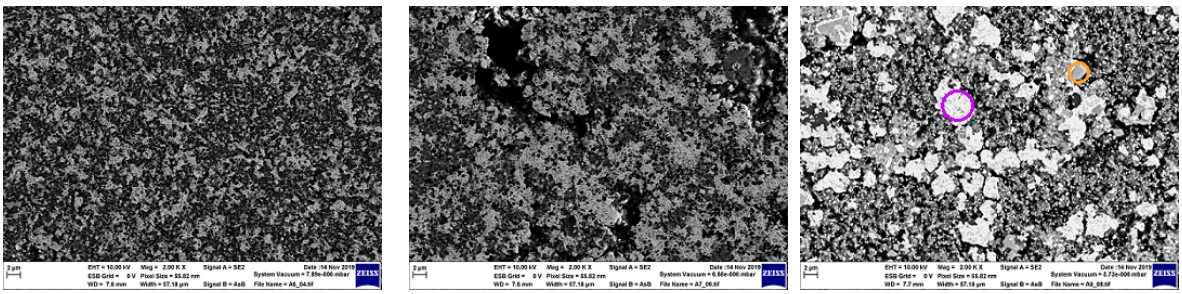

Figure 4.23: Proceeding Ag-deposition in $Ag_{3.4}$ZSP with increasing temperature: 900 °C (left); 1000 °C (middle); 1100 °C (right)

Table 4.5: EDX measurements of $Ag_{3.4}ZSP$ annealed at 1100 °C

	amount [wt-%]						
Spectrum	**O**	**Na**	**Si**	**P**	**Zr**	**Ag**	**Total**
1	3.32	0	0.36	0	1.94	94.37	100
2	35.22	0	13.7	0	51.08	0	100
3	40.03	0	20.3	0	37.85	1.83	100
Ag3.4ZSP	**23.21**	**0**	**8.15**	**2.25**	**22.06**	**44.34**	**100**
ZrSiO4	**34.91**		**15.32**		**49.77**		**100.00**

The obtained EDX spectra and close-up pictures of the microstructures confirm, that like Ag_3ZSP,[75] also $Ag_{3.4}ZSP$ slowly starts to decompose in a temperature range between 700 an 800 °C. First, side phases with a high concentration of Ag could be observed, whereas at even higher temperatures, metallic Ag and $ZrSiO_4$ start to segregate. For a more accurate determination of this decomposition process, more investigations would need to be carried out.

4.3.5 Electrical Studies

Since sintering needs to be depressed to temperatures of 700 °C or lower, to prohibit the degradation of $Ag_{3.4}ZSP$, no dense pellets of the material could be prepared. In addition, the samples sintered at 600 and 700 °C showed a high degree of broad reflexes, which is why an analysis and distinct assignment of the space groups for these spectra was not possible. Therefore, the dielectric properties of the different pellets were for now only analysed qualitatively at RT to determine the impact of the side phases on the respective resistances.

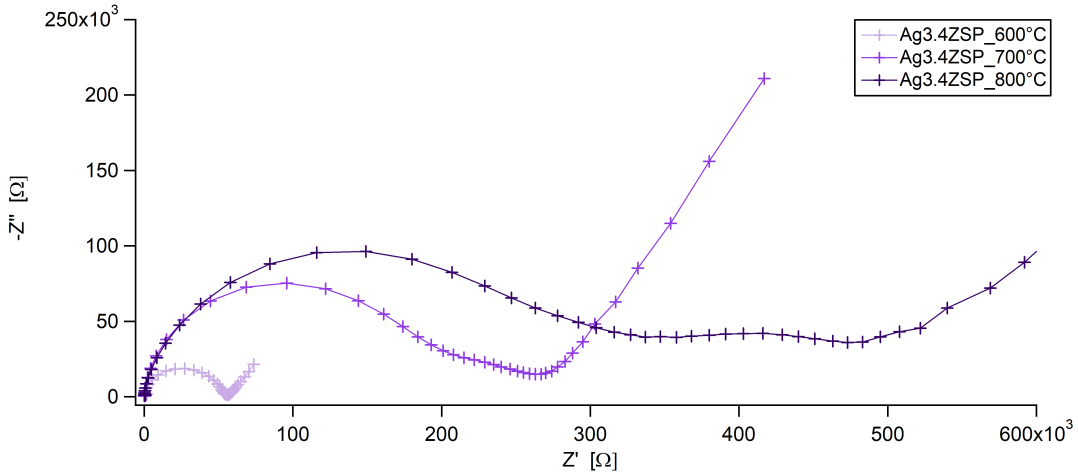

Figure 4.24: Nyquist plots of $Ag_{3.4}ZSP$ sintered at temperatures of 600 °C, 700 °C and 800 °C

A comparison of the obtained Nyquist plots displayed in Figure 4.24 shows, that as a result of the decomposition process, the total resistance increases significantly, and an additional side contribution becomes visible. At temperatures of 900 °C and higher, the dielectric properties of the pellets could not be accessed, as all of them showed an internal short circuit, which most presumably can be traced back to the segregation of metallic Ag.

4.4 LZSP

Equally to K_3ZSP, the crystal structure of Li_3ZSP was reported and analysed by Hong and Goodenough,[21] which is why the first synthesis was carried out with this stoichiometry. Since a higher charge carrier concentration can lead to higher ionic conductivities and no literature is available concerning this stoichiometry, the synthesis of $Li_{3.4}$ZSP and $Li_{3.4}$ZSP (2%Nb) was attempted as well to allow for later comparison to the K-, Ag- and Na-based analogues.

4.4.1 Visual Characterisation

Figure 4.25 shows pellets of Li_3ZSP sintered at 950 °C and $Li_{3.4}$ZSP sintered at 900 °C for 12 h. The samples obtained for Li_3ZSP exhibit a slightly grey colour, whereas the ones for $Li_{3.4}$ZSP are completely white. In contrast to $Li_{3.4}$ZSP and $Li_{3.4}$ZSP (2%Nb), green bodies of Li_3ZSP were additionally treated at temperatures of 1100 °C and 1250 °C. In the first case, the pellets did show lots of cracks, whereas in the second case, compact pellets could be obtained.

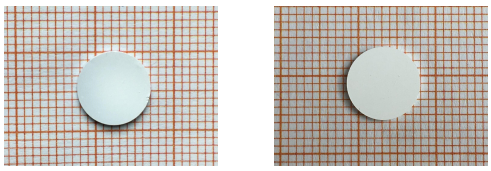

Figure 4.25: Pellets of Li_3ZSP (950 °C) and $Li_{3.4}$ZSP (900 °C)

4.4.2 XRD analysis

The XRD patterns of Li_3ZSP and $Li_{3.4}$ZSP treated at various different sintering temperatures can be found in Figure 4.26. In the case of Li_3ZSP, the screening shows that a minimum heat of 1000 °C is necessary to obtain a crystalline phase. As the temperature is increased to 1250 °C, smaller reflexes, possibly originating from side phases, disappear. The spectra obtained from the different $Li_{3.4}$ZSP-samples show the same trends as the ones from $K_{3.4}$ZSP. Like in the case for the K-based analogues, more narrow reflexes can be observed at 1000 °C compared to 900 °C, indicating a higher degree of crystallinity. The addition of Nb once more shifted the intensities of the respective reflexes, but not their positions.

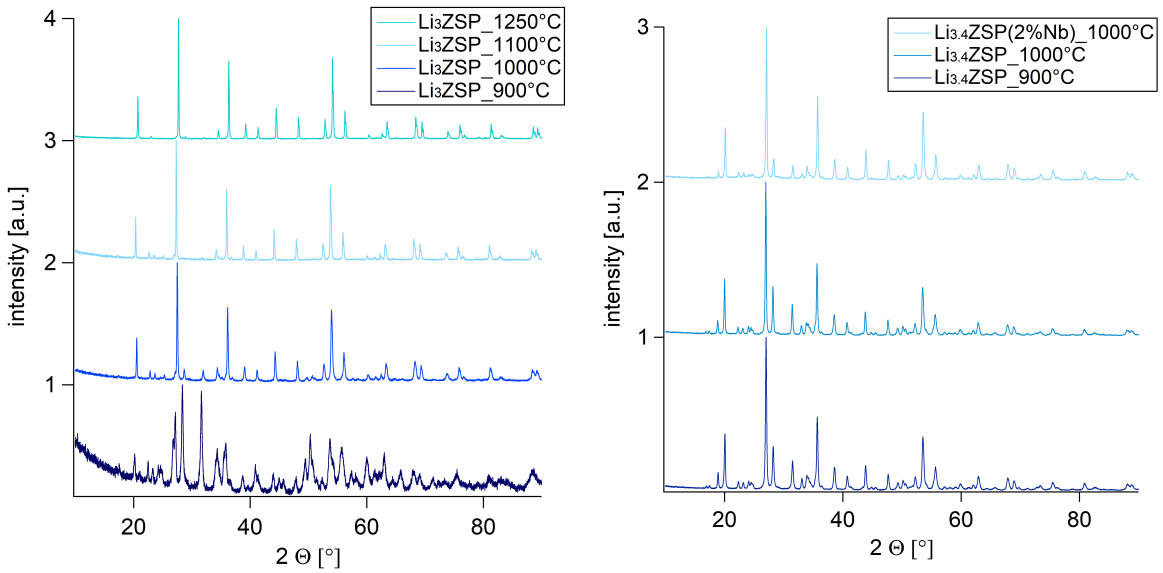

Figure 4.26: Influence of the sintering temperature on the measured XRD patterns of Li_3ZSP (left) and $Li_{3.4}ZSP$ (right)

For further crystal structure examinations, the measured patterns of Li_3ZSP at 1250 °C and $Li_{3.4}ZSP$ at 1000 °C were used. Like for the K-based analogues, the space group $P2_1/c$ seems to give the best fit for both stoichiometries (see Figure 4.27 and 4.28). As one can see, the experimentally obtained spectrum of Li_3ZSP correlates well with the calculated fit and no side phases could be observed. Analysis of the spectra obtained for $Li_{3.4}ZSP$ show, that a small amount of ZrO_2 (dark-orange) seems to be present within the sample.

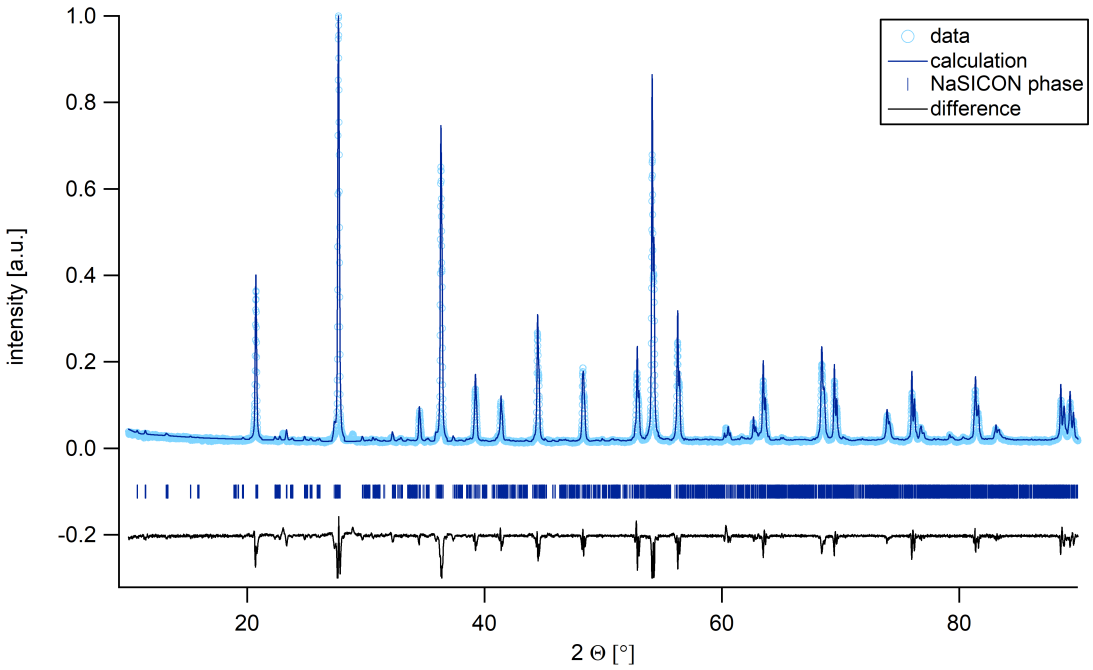

Figure 4.27: XRD pattern of Li_3ZSP at 1250 °C with proposed fit

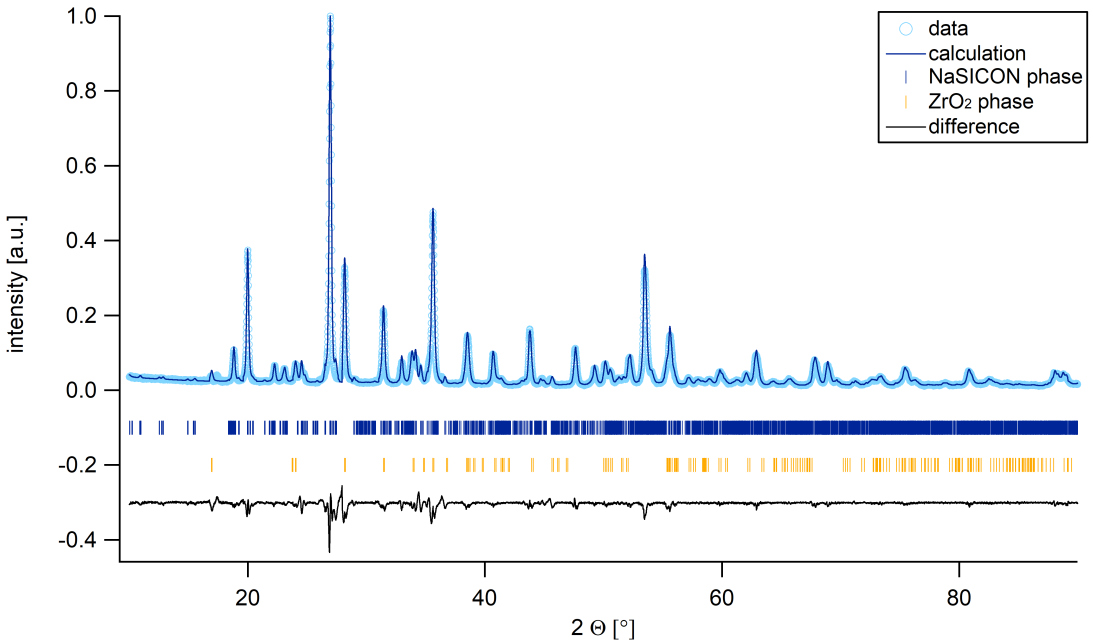

Figure 4.28: XRD pattern of $Li_{3.4}ZSP$ at 1000 °C with proposed fit

Since the main goal of this thesis was the synthesis of solid electrolytes for post-lithium ion batteries, and extensive investigations of K_3ZSP and $K_{3.4}ZSP$ did lead to a reassessment of the crystal structure, no further investigations of these compounds were carried out. The objective of their synthesis was mainly limited to a later comparison of the ion dynamics. In order to see, whether $Li_{3.4}ZSP$ can be synthesised phase-pure *via* solid state route, further revisions of the synthesis route and investigations like in the case of $K_{3.4}ZSP$ have to be carried out.

4.5 Ion exchange experiments

Although, the Li- and Ag-based analogues of Na_3ZSP could be synthesised, the obtained monoclinic phases are not as preferable as the rhombohedral ones like already mentioned in Section 1.3. Therefore, further ion exchange experiments were carried out with sintered $Na_{3.4}ZSP$-powder, prepared with excess Na_2CO_3 and $NH_4H_2PO_4$.

4.5.1 XRD analysis

Figure 4.29 shows the XRD patterns of the calcined and sintered sample in comparison to $Na_{3.35}ZSP$ with the crystal structure *R*-3*c* (taken from ICSD #62386) since the exact same composition was not listed in this database. Besides some minor deviations, all main reflexes can be assigned to the intended rhombohedral phase.

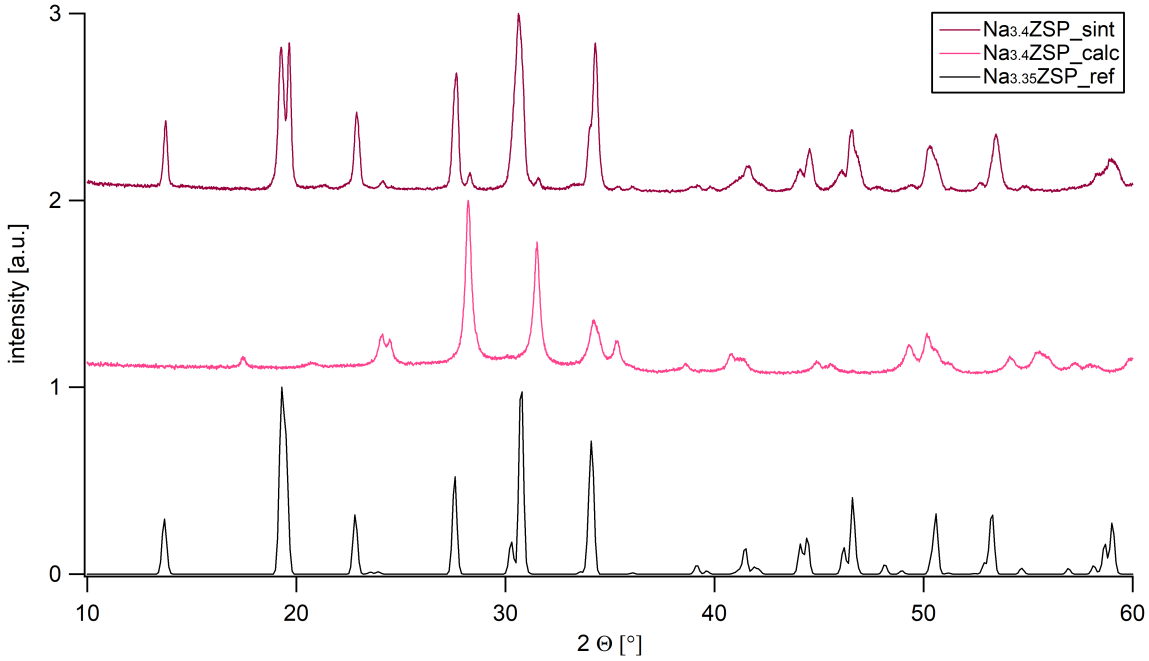

Figure 4.29: XRD patterns of the calcined and sintered $Na_{3.4}ZSP$-samples in comparison to ICSD # 62386

$Na_{3.4}ZSP$ was not analysed any further but only used for subsequent synthesis of $K_{3.4}ZSP$, $Ag_{3.4}ZSP$ and $Li_{3.4}ZSP$. After ion exchange in the respective molten salts for 24 h, different XRD patterns were obtained for each batch, indicating that a certain degree of the Na-ions could successfully be exchanged (see Figure 4.30 on the left). Additionally, pellets of these samples were sintered at 1250 °C ($K_{3.4}ZSP$ and $Li_{3.4}ZSP$) and 700 °C ($Ag_{3.4}ZSP$) to see, if their density can be enhanced as shown on the right side. Besides for $Ag_{3.4}ZSP$, completely different XRD patterns were obtained, resulting either from a phase transition or decomposition.

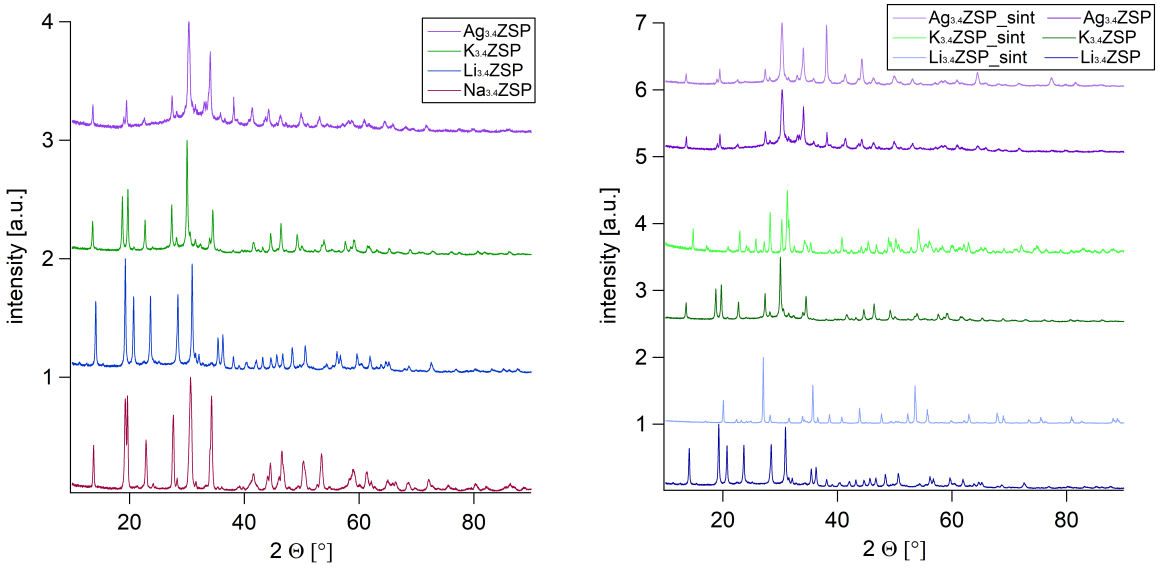

Figure 4.30: Comparison of the XRD patterns of sintered $Na_{3.4}ZSP$ exchanged in molten KNO_3, $LiNO_3$ and $AgNO_3$ (left); changes of XRD patterns after sintering at 1250 °C (right)

When looking at these graphs and the following interpretation, it has to be noted, that these are preliminary results and evaluations. To confirm an ion exchange close to 100 %, additional analysis needs to be carried out in form of e.g. ICP-OES and EDX measurements. Nonetheless, first assignments of the obtained patterns were carried out for each sample. The following table 4.6 gives an overview of the space groups, providing the best fits for the respective compounds. The corresponding graphs can be found in the appendix (Figures 8.4 to 8.6).

Table 4.6: Proposed space groups for the ion exchanged samples before and after sintering

before sintering		*after sintering*	
sample	**assigned space group**	**sample**	**assigned space group**
$Ag_{3.4}ZSP$	$C2/c$	$Ag_{3.4}ZSP$	$C2/c$
$K_{3.4}ZSP$	$R\text{-}3c$	$K_{3.4}ZSP$	$C2/c$
$Li_{3.4}ZSP$	$C2/c$	$Li_{3.4}ZSP$	$C2/c$

5 Conclusion and Outlook

The aim of this thesis was the synthesis and analysis of solid state electrolytes for post-lithium ion batteries. Therefore, several different approaches were pursued in order to prepare the Ag- and K-based analogues of the Na Super Ionic CONductor (NaSICON) with the overall formula $Na_{1+x}Zr_2Si_xP_{3-x}O_{12}$ (NZSP) for x=2 and/or x=2.4.

First synthesis attempts of the K-based materials $K_3Zr_2Si_2PO_{12}$ (K_3ZSP), $K_{3.4}Zr_2Si_{2.4}P_{0.6}O_{12}$ ($K_{3.4}$ZSP) and $K_{3.36}Zr_{1.96}Nb_{0.04}Si_{2.4}P_{0.6}O_{12}$ ($K_{3.4}$ZSP (2%Nb)) were carried out *via* solid state route and several different adjustments of the calcination/sintering process as well as the starting mixtures were made. Results of Powder X-Ray Diffraction (PXRD) and Scanning Electron Microscopy (SEM) measurements suggest, that the crystal lattice of the desired composition is too small to accommodate all the K-ions in the structure. Therefore, a crystal structure revision was conducted and Si replaced by P. The resulting compound $KZr_2(PO_4)_3$ (KZP), could be synthesised phase-pure and crystallised in the rhombohedral structure (R-3c). Electrical Impedance Spectroscopy (EIS) studies revealed, that the overall conductivity is enhanced to a great extent by moisture and that the measured ionic conductivity at 230 °C amounts to 2.04E-10 S/cm, whereas the activation energy of this process lies at 0.83(1) eV.

For the second approach, phase-pure $Na_{3.4}$ZSP was prepared *via* solid state route and the Na-ions afterwards exchanged by Ag-, K- and Li-ions in solution or melt. Also here, Le Bail fits were proposed for each compound prior to, as well as after re-sintering. The preliminary space group assignments show, that despite for $K_{3.4}$ZSP, which could be assigned the rhombohedral space group R-3c before the heat treatment, all others exhibit the monoclinic $C2/c$ space group. Like the K-based NaSICON materials, also sintered $Ag_{3.4}$ZSP was further investigated *via* Simultaneous Thermal Analysis (STA) and SEM. It could be concluded, that like the x=2-stoichiometry, the material decomposes in a temperature range between 700 and 800 °C and with further increasing sintering temperatures, Ag and $ZrSiO_4$ start to segregate. EIS studies of all samples showed an increase of the total resistance with increasing temperature in the range of 600 to 800 °C. Samples sintered at 900 °C and above, could not be characterised as they showed internal short circuits, most presumably related to the depositions of Ag. An overview of all prepared samples with the attempted synthesis routes as well as the chosen analysis methods and respective characterisations can be found in the appendix (see Table 8.3).

The results of this thesis should be viewed as a starting point for the preparation of solid state electrolytes based on alternate, rarely investigated chemistries. After the proper analysis of $KZr_2(PO_4)_3$, now different substitutions of the Zr-ions (e.g. with La) can be explored, their influence on the crystal lattice analysed and the ionic conductivities of the material increased. As a higher ion concentration in the crystal structure can increase the ionic conductivity of solid state electrolytes, the stoichiometry of $Ag_{3.4}$ZSP should be revised to try and find an optimum composition where the material crystallises in the rhombohedral phase without any additional side phases and dense pellets can be obtained after sintering. Upcoming experiments need to be directed toward optimising the stoichiometries of the crystal lattice for the K-ion and the Ag-ion, while also finding an ideal mobile ion carrier concentration.

6 References

[1] Reiner Korthauer. *Handbuch Lithium-Ionen-Batterien*. Springer, 2013.

[2] Xiaosong Hu, Changfu Zou, Caiping Zhang, and Yang Li. "Technological developments in batteries: a survey of principal roles, types, and management needs". In: *IEEE Power and Energy Magazine* 15.5 (2017), pp. 20–31.

[3] Prasant Kumar Nayak, Liangtao Yang, Wolfgang Brehm, and Philipp Adelhelm. "From lithium-ion to sodium-ion batteries: advantages, challenges, and surprises". In: *Angewandte Chemie International Edition* 57.1 (2018), pp. 102–120.

[4] M Guin and F Tietz. "Survey of the transport properties of sodium superionic conductor materials for use in sodium batteries". In: *Journal of power sources* 273 (2015), pp. 1056–1064.

[5] Dipan Kundu, Elahe Talaie, Victor Duffort, and Linda F Nazar. "The emerging chemistry of sodium ion batteries for electrochemical energy storage". In: *Angewandte Chemie International Edition* 54.11 (2015), pp. 3431–3448.

[6] Peter J Hall and Euan J Bain. "Energy-storage technologies and electricity generation". In: *Energy policy* 36.12 (2008), pp. 4352–4355.

[7] Eskinder D Gemechu, Guido Sonnemann, and Steven B Young. "Geopolitical-related supply risk assessment as a complement to environmental impact assessment: the case of electric vehicles". In: *The International Journal of Life Cycle Assessment* 22.1 (2017), pp. 31–39.

[8] Theodosios Famprikis, Pieremanuele Canepa, James A Dawson, M Saiful Islam, and Christian Masquelier. "Fundamentals of inorganic solid-state electrolytes for batteries". In: *Nature materials* (2019), pp. 1–14.

[9] J-M Tarascon and Michel Armand. "Issues and challenges facing rechargeable lithium batteries". In: *Materials for Sustainable Energy: A Collection of Peer-Reviewed Research and Review Articles from Nature Publishing Group*. World Scientific, 2011, pp. 171–179.

[10] Yoshinori Noguchi, Eiji Kobayashi, Larisa S Plashnitsa, Shigeto Okada, and Jun-ichi Yamaki. "Fabrication and performances of all solid-state symmetric sodium battery based on NASICON-related compounds". In: *Electrochimica Acta* 101 (2013), pp. 59–65.

[11] Christian Julien and Gholam-Abbas Nazri. *Solid state batteries: materials design and optimization*. Vol. 271. Springer Science & Business Media, 2013.

[12] Alexandre Ponrouch and M Rosa Palacín. "Post-Li batteries: promises and challenges". In: *Philosophical Transactions of the Royal Society A* 377.2152 (2019), p. 20180297.

[13] Romain Dugas, Juan D Forero-Saboya, and Alexandre Ponrouch. "Methods and protocols for reliable electrochemical testing in post-Li batteries (Na, K, Mg, and Ca)". In: *Chemistry of Materials* 31.21 (2019), pp. 8613–8628.

[14] Jeffrey W Fergus. “Ceramic and polymeric solid electrolytes for lithium-ion batteries”. In: *Journal of Power Sources* 195.15 (2010), pp. 4554–4569.

[15] Jürgen Janek and Wolfgang G Zeier. “A solid future for battery development”. In: *Energy* 500.400 (2016), p. 300.

[16] Kazuo Murata, Shuichi Izuchi, and Youetsu Yoshihisa. “An overview of the research and development of solid polymer electrolyte batteries”. In: *Electrochimica acta* 45.8-9 (2000), pp. 1501–1508.

[17] Lukas Porz, Tushar Swamy, Brian W Sheldon, Daniel Rettenwander, Till Frömling, Henry L Thaman, Stefan Berendts, Reinhard Uecker, W Craig Carter, and Yet-Ming Chiang. “Mechanism of lithium metal penetration through inorganic solid electrolytes”. In: *Advanced Energy Materials* 7.20 (2017), p. 1701003.

[18] Qianli Ma, Chih-Long Tsai, Xian-Kui Wei, Marc Heggen, Frank Tietz, and John TS Irvine. “Room temperature demonstration of a sodium superionic conductor with grain conductivity in excess of 0.01 S cm- 1 and its primary applications in symmetric battery cells”. In: *Journal of Materials Chemistry A* 7.13 (2019), pp. 7766–7776.

[19] Yanli Ruan, Fang Guo, Jingjing Liu, Shidong Song, Ningyi Jiang, and Bowen Cheng. “Optimization of Na3Zr2Si2PO12 ceramic electrolyte and interface for high performance solid-state sodium battery”. In: *Ceramics International* 45.2 (2019), pp. 1770–1776.

[20] John B Goodenough, HY-P Hong, and JA Kafalas. “Fast Na+-ion transport in skeleton structures”. In: *Materials Research Bulletin* 11.2 (1976), pp. 203–220.

[21] HY-P Hong. “Crystal structures and crystal chemistry in the system Na1+ xZr2SixP3- xO12”. In: *Materials Research Bulletin* 11.2 (1976), pp. 173–182.

[22] N Anantharamulu, K Koteswara Rao, G Rambabu, B Vijaya Kumar, Velchuri Radha, and M Vithal. “A wide-ranging review on Nasicon type materials”. In: *Journal of materials science* 46.9 (2011), pp. 2821–2837.

[23] Youichi Shimizu, Yasunori Azuma, and Satoko Michishita. “Sol–gel synthesis of NASICON discs from aqueoussolution”. In: *Journal of Materials Chemistry* 7.8 (1997), pp. 1487–1490.

[24] Lukas Ladenstein, Sarah Lunghammer, Eric Wang, Lincoln J Miara, Martin Wilkening, Guenther J Redhammer, and Daniel Rettenwander. “On the dependence of ionic transport on crystal orientation in NaSICON-type solid electrolytes”. In: *Journal of Physics: Energy* (2020).

[25] M Barj, H Perthuis, and Ph Colomban. “Relations between sublattice disorder, phase transitions and conductivity in NASICON”. In: *Solid State Ionics* 9 (1983), pp. 845–850.

[26] Brian L Cushing and John B Goodenough. “Li2NaV2 (PO4) 3: A 3.7 V lithium-insertion cathode with the rhombohedral NASICON structure”. In: *Journal of Solid State Chemistry* 162.2 (2001), pp. 176–181.

[27] Sahir Naqash, Frank Tietz, and Olivier Guillon. “Synthesis and characterization of equimolar Al/Y-substituted NASICON solid solution Na1+ 2x+ yAlxYxZr2- 2xSiyP3- yO12”. In: *Solid State Ionics* 319 (2018), pp. 13–21.

[28] Enrique R Losilla, Miguel AG Aranda, Sebastián Bruque, Miguel A Paris, Jesus Sanz, and Anthony R West. “Understanding Na mobility in NASICON materials: a Rietveld, 23Na and 31P MAS NMR, and impedance study”. In: *Chemistry of materials* 10.2 (1998), pp. 665–673.

[29] RS Gordon, GR Miller, BJ McEntire, ED Beck, and JR Rasmussen. “Fabrication and characterization of Nasicon electrolytes”. In: *Solid State Ionics* 3 (1981), pp. 243–248.

[30] Huifang Fei, Yining Liu, Yongling An, Xiaoyan Xu, Guifang Zeng, Yuan Tian, Lijie Ci, Baojuan Xi, Shenglin Xiong, and Jinkui Feng. “Stable all-solid-state potassium battery operating at room temperature with a composite polymer electrolyte and a sustainable organic cathode”. In: *Journal of Power Sources* 399 (2018), pp. 294–298.

[31] Petr Vanysek. “Electrochemical series”. In: *CRC handbook of chemistry and physics* 8 (2000).

[32] Kaixiang Lei, Fujun Li, Chaonan Mu, Jianbin Wang, Qing Zhao, Chengcheng Chen, and Jun Chen. “High K-storage performance based on the synergy of dipotassium terephthalate and ether-based electrolytes”. In: *Energy & Environmental Science* 10.2 (2017), pp. 552–557.

[33] Chenglin Zhang, Yang Xu, Min Zhou, Liying Liang, Huishuang Dong, Minghong Wu, Yi Yang, and Yong Lei. “Potassium Prussian Blue Nanoparticles: A Low-Cost Cathode Material for Potassium-Ion Batteries”. In: *Advanced Functional Materials* 27.4 (2017), p. 1604307.

[34] Yongling An, Huifang Fei, Guifang Zeng, Lijie Ci, Baojuan Xi, Shenglin Xiong, and Jinkui Feng. “Commercial expanded graphite as a low–cost, long-cycling life anode for potassium–ion batteries with conventional carbonate electrolyte”. In: *Journal of Power Sources* 378 (2018), pp. 66–72.

[35] Virginie Viallet. “Handbook of Solid State Batteries”. In: *Journal of Applied Crystallography* 49.Pt 6 (2016), p. 2279.

[36] K Funke. “AgI-type solid electrolytes”. In: *Progress in solid state chemistry* 11 (1976), pp. 345–402.

[37] Boone B Owens and Joseph R Bottelberghe. “Twenty year storage test of Ag/RbAg4I5/I2 solid state batteries”. In: *Solid State Ionics* 62.3-4 (1993), pp. 243–249.

[38] M Venkateswarlu and N Satyanarayana. “AC conductivity studies of silver based fast ion conducting glassy materials for solid state batteries”. In: *Materials Science and Engineering: B* 54.3 (1998), pp. 189–195.

[39] E Ramesh Kumar, P Nageswar Rao, K Rajani Kumari, Nalluri Veeraiah, and B Appa Rao. “Effect of modifier on the silver based fast ion conducting glasses for solid state batteries”. In: *Journal of Materials Science: Materials in Electronics* 29.10 (2018), pp. 8446–8455.

[40] Hui Xie, John B Goodenough, and Yutao Li. “Li1. 2Zr1. 9Ca0. 1 (PO4) 3, a room-temperature Li-ion solid electrolyte”. In: *Journal of Power Sources* 196.18 (2011), pp. 7760–7762.

[41] Vishwanathan Ramar, Sunil Kumar, SR Sivakkumar, and Palani Balaya. “NASICON-type La3+ substituted LiZr2 (PO4) 3 with improved ionic conductivity as solid electrolyte”. In: *Electrochimica Acta* 271 (2018), pp. 120–126.

[42] Yutao Li, Weidong Zhou, Xi Chen, Xujie Lü, Zhiming Cui, Sen Xin, Leigang Xue, Quanxi Jia, and John B Goodenough. “Mastering the interface for advanced all-solid-state lithium rechargeable batteries”. In: *Proceedings of the National Academy of Sciences* 113.47 (2016), pp. 13313–13317.

[43] Satoshi Hasegawa, Nobuyuki Imanishi, Tao Zhang, Jian Xie, Atsushi Hirano, Yasuo Takeda, and Osamu Yamamoto. “Study on lithium/air secondary batteries—Stability of NASICON-type lithium ion conducting glass–ceramics with water”. In: *Journal of power sources* 189.1 (2009), pp. 371–377.

[44] Isabel Hanghofer, Bernhard Gadermaier, Alexandra Wilkening, Daniel Rettenwander, and Martin Wilkening. “Lithium Ion Dynamics in LiZr 2 (PO 4) 3 and Li 1.4 Ca 0.2 Zr 1.8 (PO 4) 3”. In: *Dalton Transactions* (2019).

[45] Anthony R West. *Solid state chemistry and its applications*. John Wiley & Sons, 2014.

[46] Jenny P Glusker, Mitchell Lewis, and Miriam Rossi. *Crystal structure analysis for chemists and biologists*. Vol. 16. John Wiley & Sons, 1994.

[47] Anthony Kelly and Kevin M Knowles. *Crystallography and crystal defects*. John Wiley & Sons, 2012.

[48] Walter Borchardt-Ott. *Kristallographie*. Vol. 5. Springer, 2002.

[49] Truls Norby and Per Kofstad. “Defects and transport in crystalline solids”. In: *Compendium used in the course” Defect Chemestry and Transportation” at the University of Oslo* (2007).

[50] Helmut Mehrer. *Diffusion in solids: fundamentals, methods, materials, diffusion-controlled processes*. Vol. 155. Springer Science & Business Media, 2007.

[51] Xingfeng He, Yizhou Zhu, and Yifei Mo. “Origin of fast ion diffusion in super-ionic conductors”. In: *Nature communications* 8.1 (2017), pp. 1–7.

[52] Vitalij Pecharsky and Peter Zavalij. *Fundamentals of powder diffraction and structural characterization of materials*. Springer Science & Business Media, 2008.

[53] Andrzej Lasia. *Electrochemical impedance spectroscopy and its applications*. Springer, 2014.

[54] Derek C Sinclair. “Characterisation of electro-materials using ac impedance spectroscopy”. In: *Boletín de la Sociedad Española de Cerámica y Vidrio* 34.2 (1995), pp. 55–65.

[55] GW Walter. “A review of impedance plot methods used for corrosion performance analysis of painted metals”. In: *Corrosion Science* 26.9 (1986), pp. 681–703.

[56] Andreas Jossen. “Fundamentals of battery dynamics”. In: *Journal of power sources* 154.2 (2006), pp. 530–538.

[57] Peter Keil and Andreas Jossen. “Aufbau und parametrierung von batteriemodellen”. In: *19. DESIGN&ELEKTRONIK-Entwicklerforum Batterien & Ladekonzepte*. 2012.

[58] Dirk Uwe Sauer. “Grundlagen der Impedanzspektroskopie fur die Charakterisierung von Batterien”. In: *Technische Mitteilungen* 99.1 (2006), pp. 74–80.

[59] Mark E Orazem and Bernard Tribollet. *Electrochemical impedance spectroscopy*. John Wiley & Sons, 2008.

[60] AN Pavlov, IP Raevski, TA Minasyan, SI Raevskaya, MA Malitskaya, VV Titov, D Pandey, and AA Bokov. “Polarization Switching Dynamics in PbFe 1/2 Nb 1/2 O 3 Ceramics as Seen via the Frequency Dependence of Hysteresis Loops”. In: *Advanced Materials*. Springer, 2017, pp. 167–178.

[61] Florian Preishuber-Pflügl and Martin Wilkening. “Mechanochemically synthesized fluorides: local structures and ion transport”. In: *Dalton Transactions* 45.21 (2016), pp. 8675–8687.

[62] Stefan Breuer, Denise Prutsch, Qianli Ma, Viktor Epp, Florian Preishuber-Pflügl, Frank Tietz, and Martin Wilkening. “Separating bulk from grain boundary Li ion conductivity in the sol–gel prepared solid electrolyte Li 1.5 Al 0.5 Ti 1.5 (PO 4) 3”. In: *Journal of Materials Chemistry A* 3.42 (2015), pp. 21343–21350.

[63] Jeppe C Dyre, Philipp Maass, Bernhard Roling, and David L Sidebottom. “Fundamental questions relating to ion conduction in disordered solids”. In: *Reports on Progress in Physics* 72.4 (2009), p. 046501.

[64] Alo Dutta, TP Sinha, P Jena, and S Adak. “Ac conductivity and dielectric relaxation in ionically conducting soda–lime–silicate glasses”. In: *Journal of Non-Crystalline Solids* 354.33 (2008), pp. 3952–3957.

[65] Ernest F Hairetdinov, Nikolai F Uvarov, Hitendra K Patel, and Steve W Martin. “Estimation of the free-charge-carrier concentration in fast-ion conducting Na 2 S-B 2 S 3 glasses from an analysis of the frequency-dependent conductivity”. In: *Physical Review B* 50.18 (1994), p. 13259.

[66] AK Kuriakose, TA Wheat, A Ahmad, and J Dirocco. “Synthesis, sintering, and microstructure of NASICONS”. In: *Journal of the American Ceramic Society* 67.3 (1984), pp. 179–183.

[67] Redhammer G. J. Rettenwander D. Ladenstein L. “The Enigmas Key: Revealing the Factors Controlling Phase Behavior and Ion Dynamics in NASICON-based Materials”. In: *in preparation* ().

[68] S Vinoth Rathan and G Govindaraj. “Dispersive conductivity and dielectric behavior in niobium based NASICON glasses and analysis using anomalous diffusion model”. In: *Solid State Ionics* 181.11-12 (2010), pp. 504–509.

[69] M Šljukić, B Matković, Biserka Prodić, and D Anderson. “The crystal structure of KZr2 (PO4) 3”. In: *Zeitschrift für Kristallographie-Crystalline Materials* 130.1-6 (1969), pp. 148–161.

[70] Iwao Yamai and Toshitaka Ota. “Thermal Expansion of Homogeneous and Gradient Solid Solutions in the System KZr2 (PO4) 3 KTi2 (PO4) 3”. In: *Journal of the American Ceramic Society* 75.8 (1992), pp. 2276–2282.

[71] Toshitaka Oota and Iwao Yamai. “Thermal Expansion Behavior of NaZr2 (PO4) 3Type Compounds”. In: *Journal of the American Ceramic Society* 69.1 (1986), pp. 1–6.

[72] K Nomura, S Ikeda, K Ito, and H Einaga. “Ionic conduction behavior in zirconium phosphate framework”. In: *Solid State Ionics* 61.4 (1993), pp. 293–301.

[73] S Yamanaka, K Yoshioka, and M Hattori. “Unusual ionic conductivities of hydrothermally prepared MZr2 (PO4) 3 (M= Na, K)”. In: *Solid State Ionics* 40 (1990), pp. 43–47.

[74] S Lunghammer, D Prutsch, S Breuer, D Rettenwander, I Hanzu, Q Ma, F Tietz, and HMR Wilkening. “Fast Na ion transport triggered by rapid ion exchange on local length scales”. In: *Scientific reports* 8.1 (2018), pp. 1–8.

[75] Y Sadaoka, M Matsuguchi, and Y Sakai. “Electrical conduction and microstructure of Ag 2 OB 2 O 3 glass and Ag 3 Zr 2 Si 2 PO 12 composites”. In: *Journal of Materials Science Letters* 9.9 (1990), pp. 1028–1032.

7 List of Figures

8 List of Tables

List of Symbols

Table 8.1: Listing of the symbols used in this thesis

symbol	description
a, b, c	coordinates of the Cartesian coordinate system
h, k, l	lattice vectors in reciprocal space
C	Capacitance
c	concentration
D	diffusion coefficient
d	shortest distance between two planes
E_a	activation energy
FW	formula weight
G	overall free energy of system
H	enthalpy
I	current
J	flux of particles
j	imaginary unit
k_B	Boltzmann constant
N	Avogadro constant
n	order of reflection
$R_{x,y,z}$	total displacement (in x, y and z direction)
r	radius
S	entropy
T	temperature
t	time
U	voltage
V	volume
W	occupation probability
Z	coordination number
Z'	real part of impedance
Z"	imaginary part of impedance
Γ	jumping rate
Δ	difference
δ	differential
θ	angle of reflection, Bragg angle ,
λ	wavelength
ν	frequency
ν_a	attempt frequency
ρ	density
σ	conductivity
τ	jump time
ω	jump rate
∇	Nabla operator

List of Abbreviations

Table 8.2: Listing of the abbreviations used in this thesis

acronym	**description**
AC	Alternating Current
AZSP	$Ag_{1+x}Zr_2Si_xP_{3-x}O_{12}$
DC	Direct Current
DTA	Differential Thermal Analysis
DTG	Derivative Thermogravimetry
EDX	Energy Dispersive X-Ray Spectroscopy
EIS	Electrochemical Impedance Spectroscopy
ICSD	Inorganic Crystal Structure Database
KZP	$KZr_2(PO_4)_3$
KZSP	$K_{1+x}Zr_2Si_xP_{3-x}O_{12}$
LZSP	$Li_{1+x}Zr_2Si_xP_{3-x}O_{12}$
NaSICON	Na Super Ionic CONductors
NZSP	$Na_{1+x}Zr_2Si_xP_{3-x}O_{12}$
(P)XRD	(Powder) X-Ray Diffraction
QMS	Quadrupole Mass Spectrometry
SEM	Scanning Electron Microscopy
SHE	Standard Hydrogen Electrode
STA	Simultaneous Thermal Analysis
TGA	Thermal Gravimetric Analysis
XRD	X-Ray Diffraction

Appendix

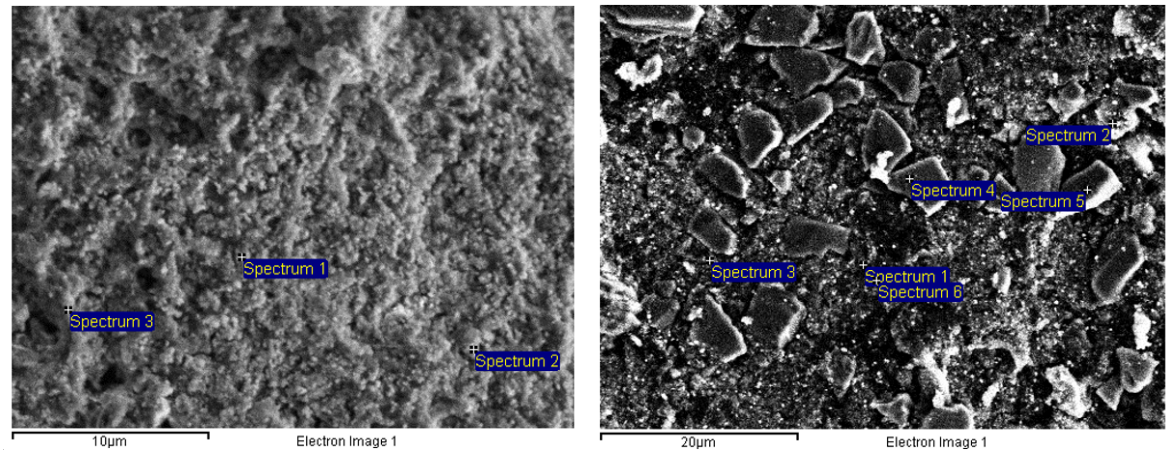

Figure 8.1: Regions of the K_3ZSP-cross-section analysed at 1000 °C (left) and of $K_{3.4}$ZSP analysed at 950 °C (right)

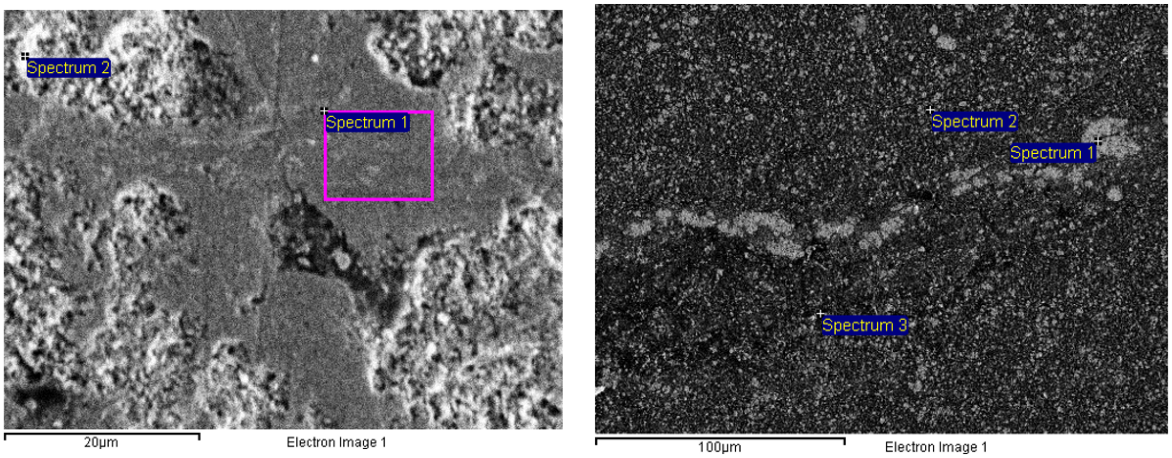

Figure 8.2: Regions of the $Ag_{3.4}$ZSP-cross-section analysed at 600 °C (left) and 800 °C (right)

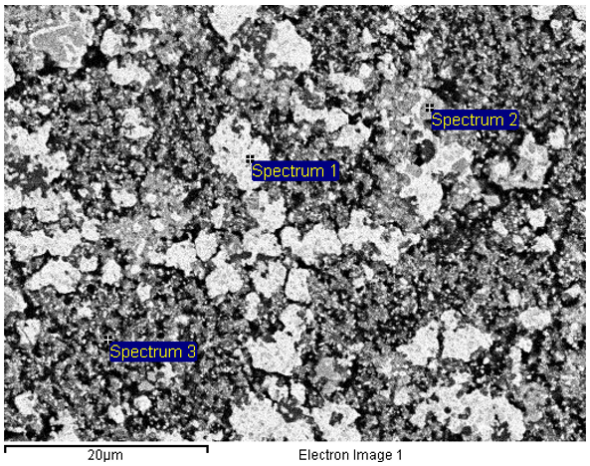

Figure 8.3: Regions of the $Ag_{3.4}$ZSP-cross-section analysed at 1100 °C

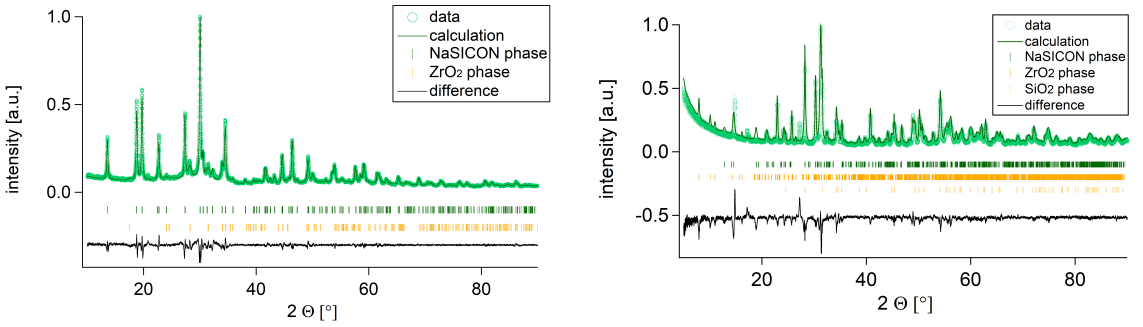

Figure 8.4: Proposed fits for $K_{3.4}$ZSP before (left) and after (right) sintering

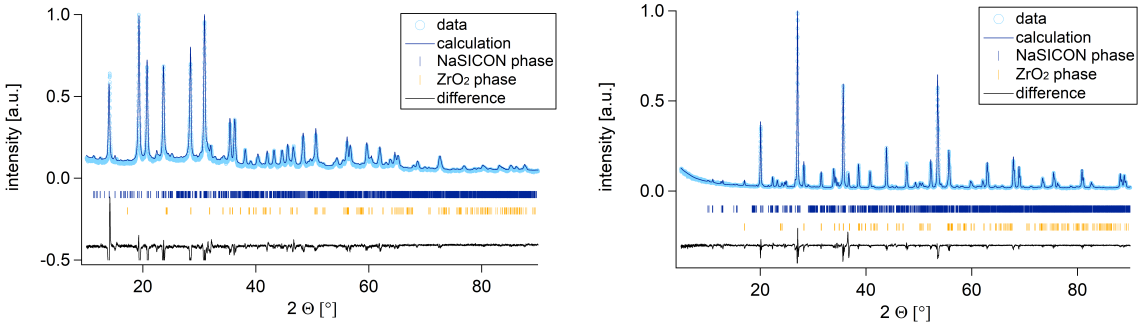

Figure 8.5: Proposed fits for $Li_{3.4}$ZSP before (left) and after (right) sintering

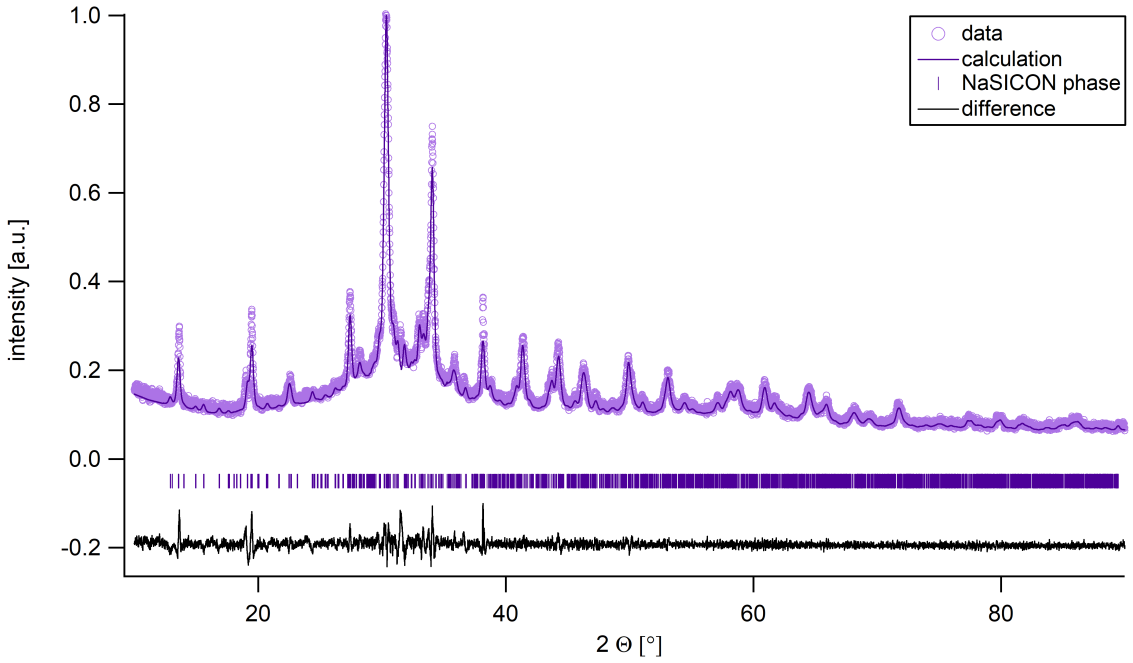

Figure 8.6: Proposed fit for $Ag_{3.4}ZSP$ after sintering

Table 8.3: Overview of samples with attempted synthesis *via* solid state route (SSR) or ion exchange (IE) as well as subsequent analyses and respective characterisations

Sample	Synthesis	Analysis	Characterisations
K_3ZSP	SSR	PXRD, STA & SEM/EDX	no EIS characterisation as analysis revealed failure of solid state synthesis & full IE could not be confirmed yet
$K_{3.4}ZSP$/ $K_{3.4}ZSP$ (2%Nb)	SSR/ IE	PXRD, STA and SEM/EDX	
KZP	SSR	PXRD	EIS in T-range of -100 to 230 °C
$Ag_{3.4}ZSP$	IE	PXRD, STA & SEM/EDX	EIS, qualitative analysis of side phase influence between 600 & 800 °C above, pellets showed short circuits
Li_3ZSP	SSR	PXRD	no further characterisation as stoichiometry of K-based analogues was revised
$Li_{3.4}ZSP$/ $Li_{3.4}ZSP$ (2%Nb)	SSR/ IE	PXRD	